Icarus 218 (2012) 1043–1070

Contents lists available at SciVerse ScienceDirect

Icarus

journal homepage: www.elsevier.com/locate/icarus

The Ashima/MIT Mars GCM and argon in the martian atmosphere

Yuan Lian [a,*], Mark I. Richardson [a], Claire E. Newman [a], Christopher Lee [a], Anthony D. Toigo [b], Michael A. Mischna [c], Jean-Michel Campin [d]

[a] Ashima Research, Suite 104, 600 South Lake Ave., Pasadena, CA 91106, USA
[b] The Johns Hopkins University, Applied Physics Laboratory, 11100 Johns Hopkins Road, Laurel, MD 20723, USA
[c] Jet Propulsion Laboratory, M/S 183-601, 4800 Oak Grove Drive, Pasadena, CA 91109, USA
[d] Massachusetts Institute of Technology, Dept. of Earth, Atmospheric, and Planetary Sciences, 54-1424, 77 Massachusetts Ave., Cambridge, MA 02139-4307, USA

ARTICLE INFO

Article history:
Received 13 October 2011
Revised 8 February 2012
Accepted 10 February 2012
Available online 22 February 2012

Keywords:
Mars
Atmospheres, Dynamics
Abundances, atmospheres

ABSTRACT

We investigate the ability of modern general circulation models (GCMs) to simulate transport in the martian atmosphere using measurements of argon as a proxy for the transport processes. Argon provides the simplest measure of transport as it is a noble gas with no sinks or sources on seasonal timescales. Variations in argon result solely from 'freeze distillation', as the atmosphere condenses at the winter poles, and from atmospheric transport. Comparison of all previously published models when rescaled to a common definition of the argon enhancement factor (EF) suggest that models generally do a poor job in predicting the peak enhancement in southern winter over the winter pole – the time when the capability of the model transport approaches are most severely tested. Despite observed peak EF values of ~6, previously published model predictions peaked at EF values of only 2–3. We introduce a new GCM that provides a better treatment of mass conservation within the dynamical core, includes more sophisticated tracer transport approaches, and utilizes a cube–sphere grid structure thus avoiding the grid-point convergence problem at the pole that exists for most current Mars GCMs. We describe this model – the Ashima Research/Massachusetts Institute of Technology Mars General Circulation Model (Ashima/MIT Mars GCM) and use it to demonstrate the significant sensitivity of peak EF to the choices of transport approach for both tracers and heat. We obtain a peak EF of 4.75 which, while over 50% higher than any prior model, remains well short of the observed value. We show that the polar EF value in winter is primarily determined by the competition between two processes: (1) mean meridional import of lower-latitude air not enriched in argon and (2) the leakage of enriched argon out of the polar column by eddies in the lowest atmospheric levels. We suggest possibilities for improving GCM representation of the CO_2 cycle and the general circulation that may further improve the simulation of the argon cycle. We conclude that current GCMs may be insufficient for detailed simulation of transport-sensitive problems like the water cycle and potentially also the dust cycle.

1. Introduction

In the absence of CO_2 condensation on Mars, completely passive tracers with no surface or photochemical sources or sinks would be well mixed and maintain constant mass mixing ratios (mmrs) over the course of the annual cycle. On Mars, however, the significant decline in the high-latitude winter atmospheric temperatures during polar night results in roughly 25% of the main atmospheric constituent, CO_2, cycling into and out of the seasonal caps yearly. This process respectively enriches and dilutes non-condensable gases with respect to the background atmosphere, and mimics "sources" and "sinks" of volatiles in the polar caps. With the advent of the Mars Odyssey Gamma Ray Spectrometer (GRS), the resultant cycling of non-condensable volatiles has been observed for the noble gas argon (Ar), the second most abundant of the non-condensable species in the martian atmosphere (Sprague et al., 2007). To be more precise, lacking sources and sinks (on seasonal time scales), the Ar abundance *at any given location* on the planet varies as a result of only two processes: the precise location and rates of CO_2 condensation or sublimation, and the atmospheric mixing and transport of volatiles across the resultant gradients. Since the CO_2 condensation cycle is one of the best-modeled aspects of the martian climate system (though whether it is good enough is something that Ar measurements have brought into question), the GRS observations give great hope of direct diagnosis of atmospheric transport and the testing of general circulation models (GCMs) (Nelli et al., 2007).

GCMs provide the most complete representations of the martian climate system (Leovy, 2001). For some aspects of the martian

* Corresponding author.
E-mail address: lian@ashimaresearch.com (Y. Lian).

0019-1035/$ - see front matter © 2012 Elsevier Inc. All rights reserved.
doi:10.1016/j.icarus.2012.02.012

climate, extremely accurate approaches to transport within these GCMs are not necessary. For example, reasonable agreement with zonal mean temperature cross-sections and lander-based surface pressure measurements are possible using even simple transport schemes because the martian atmosphere is very strongly forced by radiative heating (Leovy and Mintz, 1969; Wood and Paige, 1992). Indeed, errors in the description of dust, which dominates uncertainty in radiative heating, are likely the most significant cause for concern for simulation of the zonal mean climate (Lee et al., 2011). However, for climate components like the water cycle, and for the study of trace markers of geological and biological activity such as methane, the fidelity of atmospheric transport is very much more important. Before the advent of argon measurements by the GRS, there was no direct way to test model representations of transport. The main purpose of this paper is to introduce and test more sophisticated representations of tracer transport in GCMs and to assess how far we remain from validating our quantitative understanding of crucial transport processes in the martian atmosphere.

1.1. GRS measurements of argon

The GRS instrument can measure the abundance of argon in the martian atmosphere because of gamma ray emission from ^{41}Ar decay, which in turn is locally created from neutron capture by atmospheric ^{40}Ar (Sprague et al., 2007). The output of the instrument is actually the ratio of argon to titanium (Ar/Ti), since titanium in the GRS instrument housing can also yield ^{41}Ar when irradiated with high energy neutrons and protons. The TI contribution can be assessed through other spallation reactions in the TI housing that yield different diagnostic gamma ray signatures. Finally, the variation of thermal neutrons responsible for the ^{41}Ar creation is compensated by gamma ray measurements at yet another wavelength. The final Ar/Ti ratio is then directly related to the atmospheric argon column mass density, but by an unknown constant factor.

In order to calculate the relationship between the Ar/Ti ratio and the actual column-averaged Ar mmr (*i.e.* to calibrate the measurement), Sprague et al. (2007) isolated GRS data from (roughly) the location and season of the Viking Lander 2 (VL2) direct *in situ* measurement of Ar mmr with the Gas Chromatograph Mass Spectrometer (GCMS) (Owen et al., 1977). As the GRS field of view is large and long integration periods are necessary, the region from 30°S to 60°N and time period L_s = 90–150° were used to compare with the 48°N, L_s = 135° VL2 measurement. This single point calibration required modeling of gamma ray attenuation by the atmosphere in order for it to be extended to all seasons and locations (to scale for the effect of variations in the total atmospheric column on gamma ray propagation). The end result of the calibration and modeling is a predicted value of the Ar/Ti ratio that corresponds (for each 15° latitude bin and for the zonal average) to a homogeneous atmosphere with an argon mmr of 0.0145 – the value measured at VL2 at L_s = 135° (see Fig. 6 of Sprague et al. (2007)) – and to which the observed Ar/Ti ratio can be compared.

The GRS measurements thus require a large degree of processing for a useful argon measurement to be obtained. However, the discussion of Ar/Ti ratios, spallation in the GRS housing, and gamma ray atmospheric attenuation modeling can mask just how intuitive and useful the final enhancement factor (EF) presented by Sprague et al. (2007) is and how readily it can be compared with GCM output. The observed EF is merely the ratio between the Ar mmr *measured* in the GRS field of view (or averaging bin) and the Ar mmr *measured* at VL2 at L_s = 135° (0.0145). Note that the GRS calibration assumes that the *in situ* measurement by VL2 is representative of the column-averaged mmr. By definition then, a measured EF value of 1 corresponds to a mmr that is identical to this VL2 measurement (see Appendix A). Proper comparison with GCM results requires that the GCM EF is defined as the ratio between the *modeled* Ar (or indeed any non-condensable tracer) mmr and the *modeled* value at the VL2 location and at L_s = 135°.

The definition of EF makes it both easy to calculate from GCMs and also robust against ambiguity associated with topography, season, and even the total amount of non-condensable gas in the atmosphere (in the limit of non-condensable gas being a minor constituent such that variations in the total non-condensable do not significantly modify the total mass of the atmosphere, and hence the denominator in the mmr). The fact that it is based on column-averaged mmr rather than total column abundance eliminates concern over comparing columns with different surface pressure (elevation and/or season), while the fact that it is a ratio of the mmr at a given location and time to the mmr at VL2 at L_s = 135° eliminates concerns over getting the total model inventory of non-condensable gas correct. Indeed, the EF can be calculated from any non-condensable (real or hypothetical) in a GCM. By using a ratio of ratios, the EF is independent of the nature, identity, or initial abundance of the non-condensable gas. In reality, the assumption of uniform vertical mixing of Ar and the assumption that Ar is trace in the mmr calculation (does not contribute to the denominator) will cause some error in the true assessment of the argon from EF. However, for the time being, any errors in data/model comparisons resulting from these assumptions are likely negligible compared with errors in modeled transport, as demonstrated by this work.

1.2. Comparison of GCMs and argon observations to date

Prior to this work, three different Mars GCMs have been used in an attempt to simulate the GRS EF estimations: the NASA Ames Mars GCM (Nelli et al., 2007), the LMD Mars GCM (Forget et al., 2009; Lefèvre and Forget, 2009), and the MarsWRF GCM (Guo, 2009). The GCM results, properly scaled to the definition of EF, as given above and in Appendix A, are shown in Fig. 1. The nature and rationale for the scaling of GCMs are presented in detail in Appendix A. This scaling allows the most "apples-for-apples" GCM intercomparison and enables direct GCM comparison with the GRS data from Sprague et al. (2007), assuming that the data are correct (but see concerns presented by Forget et al. (2009) and briefly addressed in Appendix A). While the scaling for each GCM is calculated separately and based on the definition of EF presented in Appendix A, the scaling results in all of the GCMs agreeing rather well from roughly L_s = 210° to L_s = 45°. This is reassuring as prior disagreements during these season were hard to reconcile with the southern polar atmosphere likely being well mixed with the rest of the atmosphere at these times. Remaining model differences relate almost entirely to the period of maximum EF over the center of the southern polar cap in late southern autumn and winter.

Fig. 1 demonstrates the difficulty of simulating the enhancement of argon in the southern polar winter atmosphere. The GRS observations show peak values of over EF = 5 from roughly L_s = 75–150°, and with a maximum value of something around EF = 6. Looking at GCM results prior to the current work, MarsWRF obtained a peak of just over EF = 2, the NASA Ames Mars GCM just over EF = 2.5, and the LMD Mars GCM just over EF = 3. While the general shape of the MarsWRF and NASA Ames Mars GCM results appear consistent with the observations, the LMD Mars GCM appears to predict the wrong trends of EF between L_s = 60–160°, with a modeled decrease in the early part of this period (when observations show an increase) and a modeled increase in the latter part (when observations show a decrease after L_s = 110–130°). However, the LMD Mars GCM appears to do a better job in increasing the EF quickly in mid-southern autumn and to remain high longer in late southern winter, in better agreement with the EF observations.

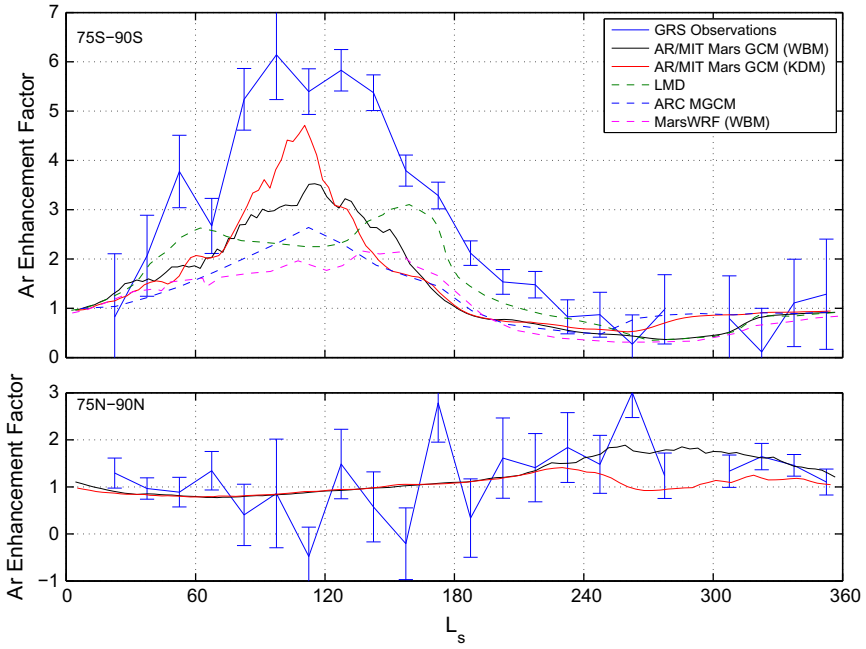

Fig. 1. Comparison of the observed and modeled argon enhancement factor (EF) for the region 75°S–90°S. All models have been scaled such that the EF is defined as the ratio of modeled argon mmr in the latitude band divided by the modeled argon at the Viking Lander 2 landing site at L_s = 135°, consistent with the GRS EF definition (Sprague et al., 2007). Blue line: GRS observations. Black line: results from the Ashima/MIT Mars GCM with the Wide Band Model (WBM) radiative transfer scheme. Red line: results from the Ashima/MIT Mars GCM with the K-Distribution Model (KDM) radiative transfer scheme. Dashed red line: Scaled LMD Mars GCM results (scaled from Forget et al. (2009) and Lefèvre and Forget (2009)). Dashed blue line: Scaled NASA Ames Mars GCM results (scaled from Nelli et al. (2007)). Dashed purple line: Scaled MarsWRF GCM results (scaled from Guo (2009)). For comparison, the lower panel shows the GRS observations and Ashima/MIT Mars GCM simulations for the northern pole (75°N–90°N).

Hence, while the GCMs clearly show that the southern polar atmosphere does retain 'freeze distilled' argon, they indicate a much less effective isolation of the southern polar vortex than recorded by the GRS data. While it has been suggested that the GRS EF calibration may be incorrect (Forget et al., 2009), the observational support for this suggestion is not especially strong (Appendix A). Overall, it seems much more likely that there are substantial failings in the representation of transport in all current Mars GCMs that are highlighted by the especially challenging environment of the southern winter polar vortex.

2. The Ashima/MIT Mars GCM

In an effort to improve our representation of tracer transport in the martian atmosphere, and thus provide more effective investigation of the argon observations, we have developed a new Mars global circulation model – the Ashima Research/Massachusetts Institute of Technology Mars General Circulation Model (Ashima/MIT Mars GCM) – to complement our existing multi-scale MarsWRF model (the martian version of the planetWRF model, Richardson et al., 2007). We chose the MITgcm (Marshall et al., 2004) as the dynamical core and combined it with the physics package from planetWRF (enabling Titan and Venus to be simulated in the MITgcm in addition to Mars, though we present only Mars results here). The MITgcm was chosen because of its finite volume dynamics, rich variety of available tracer transport schemes, and because of its cube–sphere grid structure. In this section, we briefly describe the MITgcm and the changes made to the model to allow it to simulate Mars.

2.1. Overview of the MITgcm

The MITgcm is a state of the art 3D global circulation model developed at MIT, available from http://mitgcm.org. Originally developed to simulate the atmospheric and oceanic circulations on Earth (Marshall et al., 2004), it has since been used to simulate the atmospheric circulations on Mars, Jupiter, and extra-solar planets (Zalucha et al., 2010; Lian and Showman, 2010; Showman et al., 2009). The MITgcm has several advantages over other widely-used GCMs: (1) it uses a finite volume dynamical core that provides native conservation of mass, momentum and energy, unlike the finite differencing approach used in many GCMs (including the cores for the WRF, Ames, and LMD Mars GCMs); (2), it was one of the first models to utilize curvilinear coordinates, enabling the use of a cube–sphere grid that provides more uniform resolution across the simulation domain (Adcroft et al., 2004) and specifically avoiding the polar convergence/ polar filter issue that plagues equirectangular (Plate Carree) grids; (3) it uses η coordinates in the vertical, a rescaled pressure coordinates that resolves dynamics better than traditional pressure coordinates near locations where the atmosphere or ocean intersects with topography (Adcroft and Campin, 2004); (4) it has various choices of linear and nonlinear tracer advection schemes that are designed to avoid numerical dissipation (diffusion) in different types of circulations; (5) it is highly configurable and can be easily integrated with a variety of atmospheric physics packages. In addition to these advantages, however, the MITgcm does have some limitations. It does not utilize a terrain following coordinates (such as the σ coordinates, where $\sigma = p/p_{surf}$) that is widely used in terrestrial GCMs, creating potential complexity for implementation of "physics" routines such as boundary layer mixing. It also lacks the capability to simulate a nonhydrostatic, fully compressible atmosphere as used in mesoscale capable models such as planetWRF. However, methods are available in the MITgcm to address these limitations (see Marshall et al., 1997; Molod, 2009 and Section 2.4 below). It should also be noted that the cube–sphere grid structure makes analysis of output using standard zonal mean diagnostic methods somewhat more cumbersome.

2.2. Dynamics

We solve the 3D primitive equations for atmospheric circulations in η coordinates on a sphere. The governing equations for horizontal momentum, vertical momentum, continuity and thermodynamic energy equations are (note that the forms of these governing equations are identical to those in pressure coordinates)

$$\frac{D\mathbf{v}}{Dt} + f\hat{k}\times\mathbf{v} + \nabla_p\Phi = \mathbf{F_v} \tag{1}$$

$$\frac{\partial\Phi}{\partial p} = -\frac{1}{\rho} \tag{2}$$

$$\nabla_p\cdot\mathbf{v} + \frac{\partial\omega}{\partial p} = 0 \tag{3}$$

$$\frac{D\theta}{Dt} = Q_\theta \tag{4}$$

where $\mathbf{v}$ is the horizontal wind vector, comprised of zonal wind u and meridional wind v, $\omega = dp/dt$ is vertical wind in η coordinates, Φ is geopotential, $\hat{k}$ is the unit vector in the vertical direction (positive upward), ρ is density, ∇_p is the horizontal gradient operator at a given pressure level, D/Dt is the total derivative operator given by $D/Dt = \partial/\partial t + \mathbf{v}\cdot\nabla_p + \omega\partial/\partial p$, and $\theta = T(p_0/p)^\kappa$ is potential temperature. Here T is temperature and $\kappa \equiv R/c_p$, which is a specified constant, is the ratio of the universal gas constant to the specific heat at constant pressure. The reference pressure p_0 is taken as 610 Pa (note, however, that the dynamics are independent of the choice of p_0). $\mathbf{F_v}$ represents the drag due to Reynolds stress in the turbulent planetary boundary layer or Rayleigh friction. Q_θ is rate of heating (expressed in K s^{-1}) due to diabatic processes such as radiation, turbulent mixing of heat or latent heating associated with the condensable gases such as CO_2 or H_2O. $f = 2\Omega\sin\phi$ is the Coriolis parameter, where ϕ is latitude and Ω is the rotation rate of the planet. The dependent variables $\mathbf{v}$, ω, Φ, ρ, and θ, are functions of longitude λ, latitude ϕ, pressure p, and time t.

In above equations, zonal wind u, meridional wind v in horizontal momentum equation (Eq. (1)) and potential temperature θ in thermodynamic energy equation (Eq. (4)) are solved prognostically along with the surface pressure anomaly. Density ρ in the equation of state for ideal gas, geopotential Φ in hydrostatic equation (Eq. (2)) and vertical velocity ω in continuity equation (Eq. (3)) are solved diagnostically.

2.3. Numerical discretization

The MITgcm adopts finite volume discretization in space to solve the primitive equations and tracer transport equations (Lin and Rood, 1996). The finite volume method (FVM) is superior to the finite difference method (FDM) in aspects such as conservation of mass, native discretization of momentum and energy, application of heterogeneous grids and easy adoption of multi-dimensional advection schemes. It is important to clarify the differences between the two spatial discretization methods as the latter is commonly adopted by current Mars GCM dynamical cores (also known as grid-point models). We use a tracer advection problem as an example without sinks or sources so that the conservation law applies

$$\frac{\partial}{\partial t}\int_V A\,dV + \int_S \mathbf{F}\cdot d\mathbf{S} = 0 \tag{5}$$

where A represents a tracer quantity, $\mathbf{F} = \mathbf{v}A$ is tracer flux, and $\mathbf{v}$ is wind vector. The subscripts V and S denote total volume and total surface area of a control volume (CV) respectively. For simplicity, we consider 1D transport with a centered second-order differencing scheme in a uniformly spaced grid. FDM takes the differential form of Eq. (5) and (after rearrangement) discretizes it at grid points as

$$\frac{\partial A_i}{\partial t} = -u_i\frac{A_{i+1}-A_{i-1}}{2\Delta x} - A_i\frac{u_{i+1}-u_{i-1}}{2\Delta x} \tag{6}$$

where the right-hand side of the equation is the differencing form of scalar flux $F = uA$. The FDM loses accuracy when the exact solution of tracer A or wind u has very large differences between adjacent boundaries of CVs where the gradient of F is very large (or in the case of shocks cannot be defined). It is well known that, in the extreme case of shocks, FDM either produces spurious oscillation in solutions (normally requires a filter to maintain numerical stability) or rapidly smooths the solutions depending on the spatial differencing of u and A (*e.g.* Engquist and Sjögreen, 1998). While shocks are not a typical feature of non-escaping, continuum, large-scale planetary atmospheric dynamics, sharp gradients at scales of the model grid spacing can be very important for transport problems (*e.g.* at the sharp edge of the polar vortex).

FVM, on the other hand, preserves the integral form of Eq. (5) and discretizes it as

$$\Delta x\frac{\partial\overline{A}_i}{\partial t} = -\left(F_{i+\frac{1}{2}} - F_{i-\frac{1}{2}}\right) \tag{7}$$

where $\overline{A}_i = \frac{1}{\Delta x}\int_{x_{i-\frac{1}{2}}}^{x_{i+\frac{1}{2}}} A\,dx$ is averaged over interval $\Delta x = x_{i+\frac{1}{2}} - x_{i-\frac{1}{2}}$. Note here $\overline{A}$ stands for the *space* average of A, not the *time* average used in the diagnostics of mean and eddy fluxes in Section 3.3.4. The FVM is able to resolve the discontinuity in the flux at the CV boundary by approximating the exact flux from averaged fluxes on either side of the boundary. Following Lomax et al. (2001), the flux at the boundary $i+\frac{1}{2}$ is approximated by the averaged flux at the ith and $(i+1)$ th CVs

$$F_{i+\frac{1}{2}} = \frac{1}{2}\left(\overline{(uA)}_i + \overline{(uA)}_{i+1}\right)$$

and the flux at the boundary $i-\frac{1}{2}$ is approximated by the averaged flux at the $(i-1)$ th and ith CVs

$$F_{i-\frac{1}{2}} = \frac{1}{2}\left(\overline{(uA)}_{i-1} + \overline{(uA)}_i\right)$$

where $\overline{(uA)}_i = \frac{1}{\Delta x}\int_{x_{i-\frac{1}{2}}}^{x_{i+\frac{1}{2}}} uA\,dx$. Then Eq. (7) can be expressed as

$$\Delta x\frac{\partial\overline{A}_i}{\partial t} = \frac{1}{2}\left(\overline{(uA)}_{i+1} - \overline{(uA)}_{i-1}\right) \tag{8}$$

The *spatially-averaged* approach avoids the explicit differencing of flux seen in the FDM, *i.e.*, the flux calculation is independent of grid spacing. It can also be applied to multiple boundaries of a CV simultaneously, which makes the FVM very flexible for the adoption of heterogeneous grids (as opposed to the FDM for which equally-spaced grids are desired).

2.4. Parameterization of Mars physics

We have implemented the physics package from the MarsWRF GCM in the Ashima/MIT Mars GCM. This package includes the radiative transfer schemes, surface and subsurface thermal schemes, vertical mixing scheme, a dust scheme and a simple CO_2 cycle scheme. These parameterizations of sub-grid-scale physics are known to produce satisfactory seasonal variation of dynamics on Mars when implemented in planetWRF (Richardson et al., 2007).

The MarsWRF physics package offers a choice of two radiative transfer treatments. The first scheme, the Wide-Band-Model (WBM) is actually a hybrid of schemes with direct heritage from the GFDL Mars GCM (Wilson and Hamilton, 1996; Richardson and Wilson, 2002b). The WBM accounts for the absorption and emission of thermal infrared radiation in the broad CO_2 15 μm band following Hourdin (1992), but with the addition of a non-LTE cooling approximation above roughly 60 km based on tabulated cooling rates (López-Valverde et al., 1998). The scheme also

treats absorption of incoming solar radiation in the near-infrared CO_2 bands (Burk, 1976). For dust, the scheme treats the absorption and scattering of solar insolation and infrared radiation following Briegleb (1992) and Haberle et al. (1982), respectively. The second scheme is a K-Distribution Model (KDM) (Johnson et al., 2008) that includes treatment of seven solar bands and five IR bands with varying widths. The k-distribution absorption coefficients are pre-tabulated for a wide temperature range (50–400 K) and pressure (10^{-4}–10^{6} Pa) with the potential to include other gases, such as H_2S and H_2O. These two trace gases are not currently included in our model due to their low abundances in the martian atmosphere, a few precipitable micrometers at most for H_2O and ultra-trace amount of H_2S (Farmer et al., 1976; Sprague et al., 1996). The heating rates are calculated with a two-stream solver based on the Hadley Centre Unified Model radiation code (Edwards and Slingo, 1996) that includes both the gas effects and scattering, absorption, and emission by aerosols. Since the aerosols are described purely in terms of scattering and absorption properties, any aerosol type or combination thereof can be treated with the KDM scheme.

The dust distribution input to either radiative transfer scheme may be selected as a prescribed, time-varying form following that of the "MGS dust scenario" (Forget et al., 2001; Montmessin et al., 2004) developed for and previously used by simulations included in the LMD-Oxford Mars Climate Database (Lewis et al., 1999). Alternatively, interactive and evolving dust may be directly simulated using prognostic dust lifting and transport. In this paper, we use the prescribed dust distribution to force the model.

For both the WBM and KDM radiative transfer schemes, the solar insolation at the top of the model takes into account the annual, seasonal, and diurnal cycles using current values for the length-of-year, semi-major axis, eccentricity, and argument of perihelion to calculate orbit, and the length-of-day, obliquity, and angle between perihelion and northern spring equinox to calculate planetary rotation.

The CO_2 cycle is a unique feature of the martian atmosphere. It is characterized by changes in the total atmospheric mass in response to the seasonal variation of polar temperatures that drop to the CO_2 frost point during the winter, at which point continued radiative cooling must be balanced by latent heat from condensation. Here we implement a simple scheme that successfully reproduces the Viking Lander surface pressure cycle in the MarsWRF GCM: CO_2 condenses at locations where the temperature is below the local frost point; the condensates instantly deposit on the ground and fix the surface temperature to the condensation point while present (effectively the thermal inertia becomes infinite); ground CO_2 ice thickness or mass in each grid box changes in order to balance cooling/heating in the lower atmosphere; the change of local air mass during CO_2 condensation and sublimation is treated as the change of column mass (or equivalently as a surface pressure tendency). Similar to other Mars GCMs, we assume that CO_2 condensation and sublimation only slightly modifies the total static energy and momentum and that this does not affect the large-scale dynamics. Furthermore, we ignore processes such as the sedimentation and coagulation of ice particles that would require a detailed CO_2 ice microphysics model.

We use the WRF MRF (Medium Range Forecast model) scheme to parameterize vertical turbulent mixing. In this parameterization, the turbulent kinetic energy is solved prognostically while other second order moments such as eddy momentum flux and eddy heat flux are solved diagnostically. The tendencies associated with the turbulent mixing of momentum and heat are defined as

$$\frac{\partial C}{\partial t} = \frac{\partial}{\partial z}\left[K_c\left(\frac{\partial C}{\partial z} - \gamma_c\right)\right] \tag{9}$$

where C stands for turbulent velocity, temperature or tracers. K_c is the eddy diffusion coefficient calculated in terms of stability functions in the surface layer and "local-K approach" in the rest of the PBL (Hong and Pan, 1996). γ_c stands for nonlocal effects on eddy fluxes. The first term $\frac{\partial C}{\partial t}$ of Eq. (9) provides the tendency terms $\mathbf{F_v}$ and fraction of Q_θ appeared in the governing equations for dynamics Eqs. (1) and (4) respectively.

2.5. Tracer transport schemes

Taking advantage of finite volume discretization, the MITgcm offers more options of advection schemes for tracer transport than all other current Mars GCMs. It provides traditional linear advection schemes in conjunction with Adams–Bashforth second or third-order time stepping, including a centered second or third-order upwind scheme and centered fourth-order scheme. It also offers non-linear advection schemes such as the Lax-Wendroff direct-space–time (DST) scheme and its variants, including the second-order Van Leer scheme with Superbee flux limiter (Van Leer, 1979), the second-order and third-order DST scheme (with or without flux limiting), a seventh-order one step method with monotonicity preserving limiter (Daru and Tenaud, 2004) and second-order-moment scheme (Prather, 1986). Among all these advection schemes, the linear schemes are computationally efficient but can be very diffusive. The nonlinear schemes are less diffusive in general but also require more computational time. For most tracer transport studies the positive definite schemes such as Van Leer and second-order-moment are preferred as they preclude non-physical negative mmr. Additionally, using flux limiters can effectively preserve the horizontal gradients in tracer fields without introducing spurious numerical noise.

The optimal choice of advection scheme for a given study varies with the dynamical conditions. To demonstrate how the choice of advection schemes can affect the numerical simulation results, tests of selected advection schemes have been performed using the MITgcm (Adcroft et al., 2010). These tests were based on the 1D and 2D experiments designed by Hourdin and Armengaud (1999), and included resolving a Gaussian and a step function in 1D and resolving a Gaussian feature in 2D with fixed grid resolution. These tests showed that the linear advection schemes with Adams–Bashforth time stepping are only able to resolve the Gaussian feature at very small Courant numbers (a measure of the well-known CFL instability conditions) without introducing numerical instabilities; the nonlinear DST advection schemes are more tolerant to Courant number, among which the schemes with flux limiters can better confine the amplitude of the Gaussian perturbation. The test results lead to some simple criteria for the selection of advection schemes: for low-resolution modeling, the simple linear advection schemes work satisfactorily without introducing severe numerical noise; for high-resolution modeling, higher order advection schemes are encouraged; and for atmospheric circulations associated with propagating fronts, high-order advection schemes with flux limiters are certainly required.

On Mars, waves generated by the diurnal differential heating in the upper atmosphere create large localized horizontal temperature gradients that resemble the features of propagating fronts. Under this circumstance, a high-order nonlinear advection scheme with flux limiters is preferred. However, caution must be taken to determine which advection scheme within this class to use as the scale-selective numerical diffusion may vary with location in the global circulation model. Furthermore, spatially-varying temperature actively affects the dynamics, while by contrast passive tracers are driven solely by dynamics with no feedback involved. Therefore, using a single advection scheme for both temperature and tracers may not be the best choice. As part of our study, we thus sought the optimal combination of temperature and tracer advection schemes to provide the best representation of both martian dynamics and observed tracer distributions (see Section 3.3).

2.6. Bulk atmospheric condensation and tracer mass mixing ratios

Tracer transport is also affected by the CO_2 cycle, as the latter modifies the atmospheric composition. Unlike CO_2, the passive tracer Ar does not condense in the martian atmosphere. Thus when atmospheric temperatures reach the frost point and CO_2 condenses, the resultant decrease of CO_2 mass implies an increase of Ar mmr at the same location. We can define the time varying Ar mmr in response to the CO_2 condensation as

$$q^*_{Ar} = \frac{M_{CO_2}}{M^*_{CO_2}} q_{Ar}, \tag{10}$$

where q_{Ar} is the Ar mmr, M_{CO_2} is the mass of CO_2 in a grid box and the superscript $*$ denotes the variables updated from those in the previous time step (Appendix B). Note that Ar is a passive tracer whose molecular mass does not affect the total atmospheric mass in our idealized model. This assumption is likely to be revised in future work that focuses on simulating the Ar cycle in greater detail.

2.7. Model vertical grids

The MITgcm uses η coordinates in the vertical. The top boundary condition is zero pressure and the bottom boundary is impermeable but acts as a free surface that evolves with time. A nonlinear free-surface scheme is designed to conserve tracers when vertical displacement of the bottom atmospheric layer occurs along topography (Campin et al., 2004). Both boundaries are free slip in the horizontal. The model's dynamical grid intersects the surface when it encounters raised topography. A terrain-following coordinates (*e.g.* σ coordinates, where $\sigma = p/p_{surface}$) is generally preferred for bodies with significant topography (such as Mars) to ensure the same high vertical resolution near the surface at all horizontal locations. This is mainly a concern for the model "physics" schemes, such as boundary layer mixing or radiative transfer. The MITgcm avoids this problem by using separate dynamics and physics vertical grids, allowing the insertion of additional levels into the physics grid to increase resolution in the near-surface region above topography (see Fig. 2). This also enables us to use the MarsWRF physics packages with minimal changes: in WRF each column has the same number of vertical layers above topography, whereas in the MITgcm part of the dynamical grid is below topography, so the number of vertical layers would vary horizontally without the use of a separate physics grid.

The dynamical equations (Eqs. (1)–(4)) are solved on the dynamics grid and the effect of sub-grid scale processes are calculated on the physics grid, then combined as described below. The model exchanges information and preserves consistency between the two grids using the MITgcm "GridAlt" package, which handles the interpolation of state variables (and their associated tendencies) between the fine physics grid and the coarser dynamics grid. Following Molod (2009), the total forcing of state variables on the dynamics grid is defined as

$$\left.\frac{\partial A}{\partial t}\right|^{total}_{dyn} = \left.\frac{\partial A}{\partial t}\right|^{F(dyn)}_{dyn} + \left.\frac{\partial A}{\partial t}\right|^{F(phys)}_{dyn} \tag{11}$$

where A represents state variables including potential temperature θ and horizontal velocities u and v; the subscripts *dyn* and *phys* mean the dynamics grid and physics grid respectively; and the superscripts $F(dyn)$ and $F(phys)$ mean the tendencies due to the dynamical forcing and physical forcing respectively. At the same time, the state variables also advance in time on the physics grid. The total forcing of state variables on the physics grid is defined as

$$\left.\frac{\partial A}{\partial t}\right|^{total}_{phys} = \left.\frac{\partial A}{\partial t}\right|^{F(dyn)}_{phys} + \left.\frac{\partial A}{\partial t}\right|^{F(phys)}_{phys} + \frac{A|_{dyn} - A|_{phys}}{\tau} \tag{12}$$

where τ is a timescale over which the state variables on the physics grid are relaxed to those on the dynamics grid. We choose τ equal to the dynamics time step so that the state variables on both grids are consistent at each time step.

Eqs. (11) and (12) show that the tendencies of state variables $\left.\frac{\partial A}{\partial t}\right|^{F(phys)}_{dyn}$ and $\left.\frac{\partial A}{\partial t}\right|^{F(phys)}_{phys}$ advance forward in time independently. The last term $\frac{A|_{dyn} - A|_{phys}}{\tau}$, called a correction term, maintains the consistency of state variables on both grids, which requires an interpolation from the dynamics grid to the physics grid.

For simplicity, we use the standard MITgcm "weighted approach" for the wind field state variables (Molod, 2009): for all physics levels l in dynamics level L

$$A_{phys}(l) = w(l) A_{dyn}(L) \tag{13}$$

where the weighting function $w(l)$ is designed to preserve the wind profile in the physics grid (note that δp in numerator in Eq. 8 of Molod (2009) is a typographical error), and is given by

$$w(l) = \frac{\sqrt{u(l)^2 + v(l)^2}}{\frac{1}{\Delta p(L)} \sum_l \sqrt{u(l)^2 + v(l)^2} \Delta p(l)} \tag{14}$$

where $u(l)$, $v(l)$ and $\Delta p(l)$ are the values on the physics grid from the previous time step. (Note that an initial wind profile is required to stand in for the previous time step values when the model is first started. In this case we set the initial wind profile to be constant at all physics levels, meaning that $w(l) = 1$ everywhere.)

The interpolation of temperature from the dynamics grid to the physics grid needs special treatment as inconsistencies may cause problems in the model's radiative transfer calculations as well as requiring unphysical adjustments in the planetary boundary layer. The publicly released MITgcm adopts a weighting function $w(l) = 1$ for the initialization and correction of potential temperature, meaning that the dry static energy of dynamics level L is evenly distributed over all physics levels l within the same dynamics level. This method, though simple, inevitably introduces discontinuities in the vertical temperature gradient, and we therefore choose a different approach. For the initialization of temperature on the physics grid, we preserve the vertical temperature gradient of the dynamics grid. For the correction term at each time step (the last term in Eq. (12)), we not only preserve the dry static energy in, but also the temperature gradient across, each dynamics layer (see Appendix C for details). The proper treatment of the correction term is essential as it forces the physics state to follow the dynamics state for each time step. We find our method to be superior to the "weighted approach" as the temperature across the physics

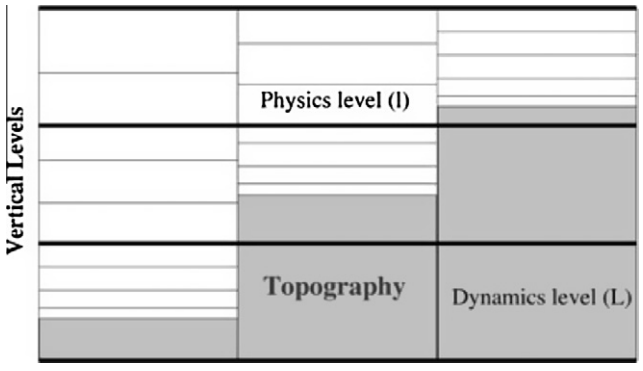

Fig. 2. Schematic plot of the physics grid (thin lines) and dynamics grid (think lines) in MITgcm. The gray areas stand for the topography. Figure courtesy of Molod (2009).

levels in adjacent dynamics levels is now closer to the dynamics state and also has a smoother profile (Fig. 3). A similar method is also applied to tracers (see Appendix C).

The interpolation of state variables in the other direction (from the fine physics grid to the coarser dynamics grid) is very straightforward and uses a simple mass weighting approach

$$A_{dyn}(L) = \frac{1}{\Delta p(L)} \sum_{l} A_{phys}(l)\Delta p(l) \tag{15}$$

This interpolation procedure is applied to both the potential temperature and wind field.

2.8. Model horizontal grids

Adopting the finite volume discretization, the MITgcm supports several gridding methods including a traditional latitude–longitude grid (also known as the equirectangular or Plate-Carree grid), a Cartesian grid (a metric-based grid that is often used to simulate regional oceanic flow at high resolution) and more advanced curvilinear grids. One of the latter, a cube–sphere grid, is of special interest as it provides nearly uniform horizontal spacing across the sphere (Fig. 4a). Traditional latitude–longitude grids (Fig. 4b) have singularities at the poles, at which gridpoints converge, and on approach to which the grid spacing in the zonal direction tends to zero. This presents a well known "pole problem", as the Courant–Friedrichs–Lewy (CFL) stability criterion requires that the model time step decrease with spacing to avoid the growth of instabilities (Fox-Rabinovitz et al., 1997; Randall, 2000). Rather than run the entire domain with small time steps, models typically use "polar filters" to smooth out model fields in these problem regions, increasing the effective model spacing there and allowing a larger time step to be used. The cube–sphere grid is thus particularly useful, as its nearly uniform spacing allows a relatively large time step to be used without requiring strong filtering of any portion of the domain. The smallest horizontal grid sizes in the cube–sphere grid appear at eight corners near 38° north and south latitude due to the projection of cubed grids onto a sphere, and the smallest grid spacing is only ~0.4 times that of the largest over the entire globe. An eighth-order Shapiro filter (Shapiro, 1970) is still applied globally to maintain numerical stability by suppressing small scale noise, as is generally required by any numerical model that does not have implicit numerical diffusion – for example, WRF has numerical diffusion designed into the numerics which provides sufficient total diffusion for the TitanWRF GCM to successfully simulate observations with no explicit horizontal diffusion whatsoever (Newman et al., 2011).

The construction of each face of the cube–sphere grid is illustrated for Mars in Fig. 5. The arrangement of the six faces close to form a cube that approximates a sphere when the grid spacing is allowed to vary across each face. Each of the faces uses an approximately polar stereographic projection. We have chosen to place the rotational poles at the center of two of these boxes, with the remaining four centered every 90° of longitude along the equator. In this sense, the cube–sphere grid can be thought of as composed of six equivalent mesoscale model domains (*c.f.* MarsWRF in mesoscale mode (Richardson et al., 2007)) with each domain edge seemed to one of its four neighbors, such that all domain boundaries are internal to the model. Fig. 5 also shows the resulting shape of the cube–sphere grid boxes when projected in regular latitude–longitude coordinates.

2.9. Model setup

The bottom boundary for the Ashima/MIT Mars GCM in this study is defined for radiative and thermal purposes with maps of albedo, thermal inertia, and emissivity defined from the MGS Thermal Emission Spectrometer (TES). For topography and for the roughness length scale in the planetary boundary layer, we use respectively the Mars Orbiter Laser Altimeter (MOLA) derived altitude referenced to the geoid and the pulse-width roughness. Maps of the topography and albedo are shown in Fig. 5 on the MITgcm cube–sphere grid for reference. All surface fields are area-weighted onto the model grid point locations from the higher-resolution data (Smith et al., 2001; Garvin et al., 1999; Mellon et al., 2000; Christensen et al., 2001).

As the MITgcm uses η coordinates, the conversion from surface elevation to surface pressure requires determination of two free

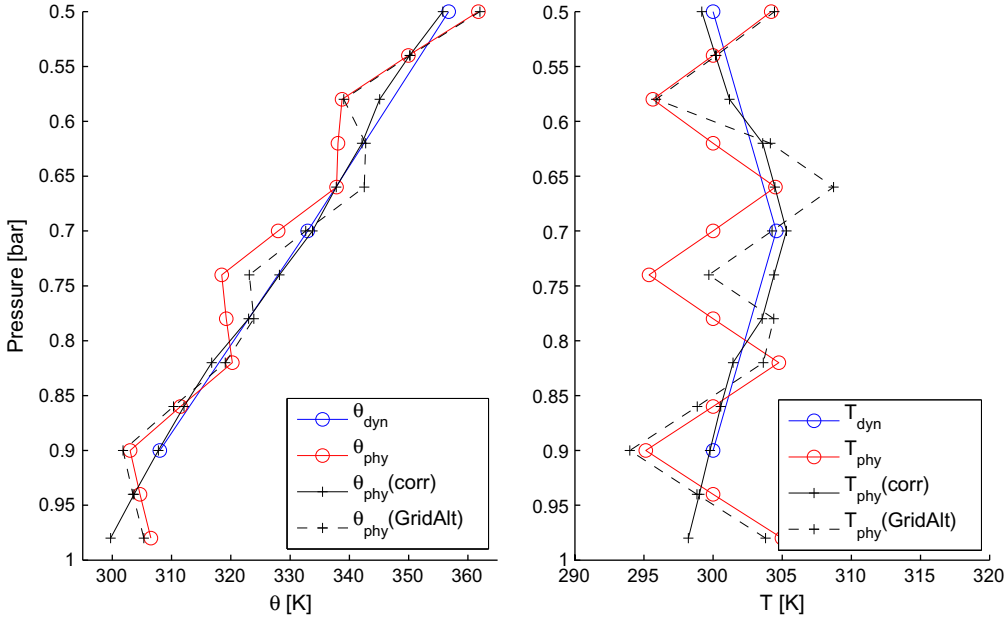

Fig. 3. Comparison between our correction of temperature in the physics grid and the one used by MITgcm "GridAlt" package. The blue line is the potential temperature (left panel) or temperature (right panel) in the dynamics grid, the red line is the potential temperature (left panel) or temperature (right panel) in the physics grid. The black solid line is the physics temperature corrected by our method. The black dashed line is the physics temperature corrected by MITgcm "GridAlt" package.

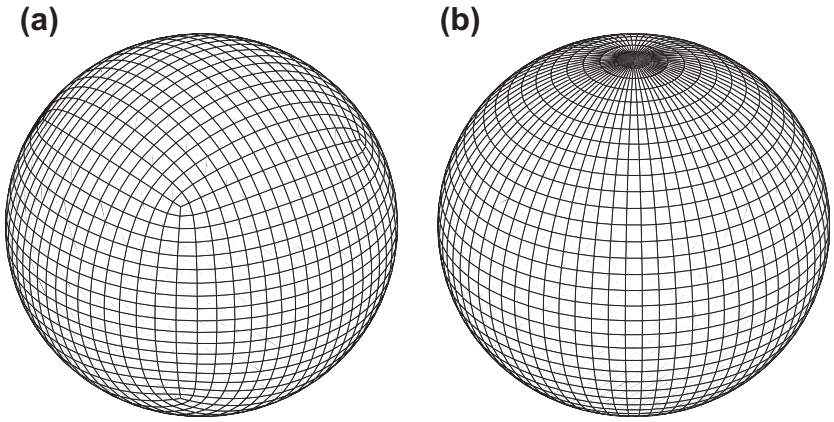

Fig. 4. Comparison between the cube–sphere grid (a) and the traditional polar-spheric grid (b). The resolution for the cube–sphere grid (a) is C18 (18×18 grid points on each of the six cube–sphere faces), equivalent to 5° resolution in the latitude–longitude grid (b).

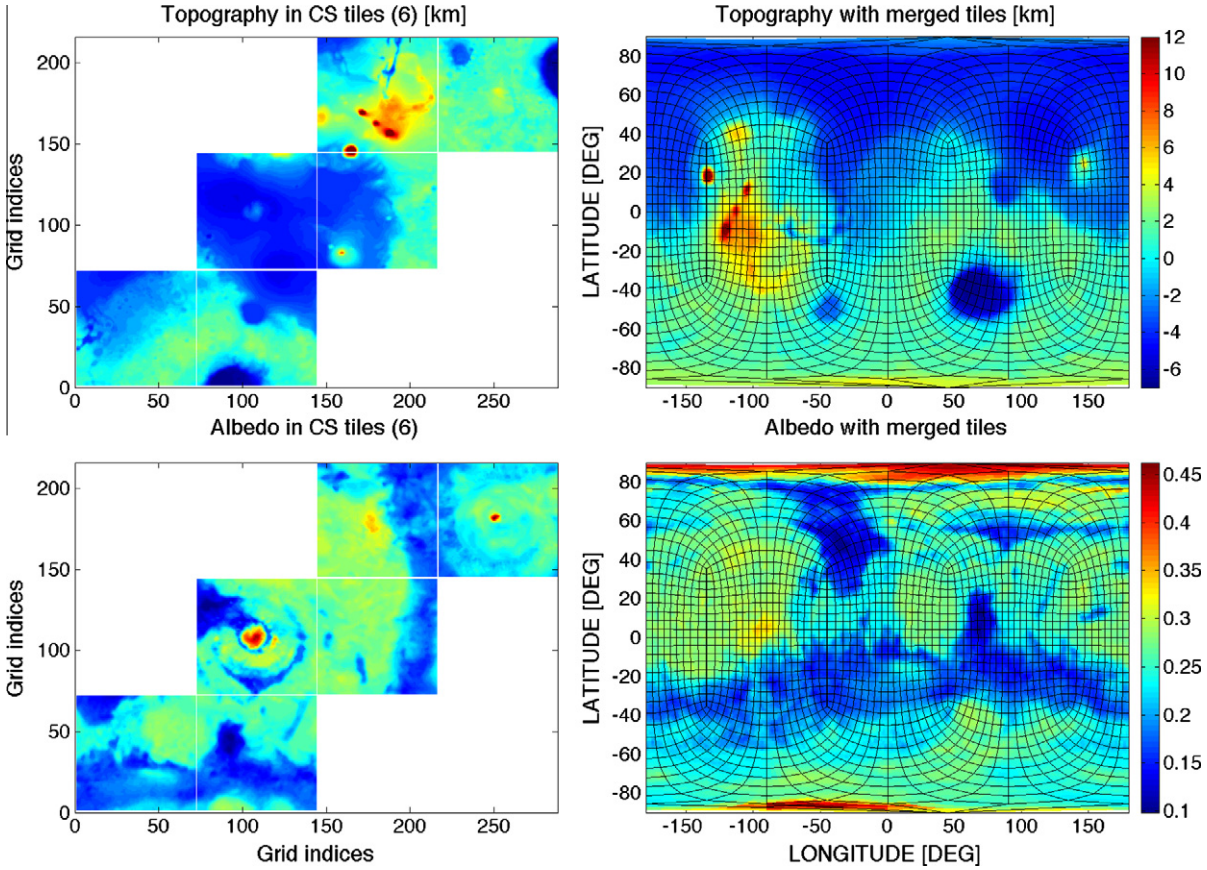

Fig. 5. The projection of topography and albedo onto the native model coordinate indices of the cube–sphere MITgcm (left top and bottom) and the projection of the cube–sphere grid onto regular latitude–longitude plots of topography and albedo (right top and bottom). The left panel shows the relationship between the global index number and the projected map for all six cube–sphere tiles. Each tile may be thought of as an equivalent mesoscale domain with roughly polar stereographic projection. The six domains are seamed along the edges to create a closed cube that approximates a sphere when the resolution of each grid cell is allowed to vary.

parameters: a prescribed reference temperature profile and a reference surface pressure (pressure at the lowest point of the topography and at the seasonal peak of the CO_2 cycle). We found that our simulation results are insensitive to the initial temperature profile, as the evolving atmospheric temperature is dominated by radiative forcing and quickly reaches a steady state. Therefore, we set the initial temperature to a very rough approximation of the reference Mars atmosphere (Leovy, 2001), which is adiabatic from the surface to 40 Pa and isothermal higher up. We then adjust the reference surface pressure to maintain the global CO_2 mass close to 2.83×10^{16} kg, a value used by the NASA Ames GCM and Mars-WRF (Haberle et al., 2008; Guo et al., 2009).

The dynamics grid contains 42 levels (WBM simulations) or 45 levels (KDM simulations) in the vertical with a reference surface pressure of 1080 Pa. From the bottom up, the layers are evenly spaced with thickness $\Delta p_{dyn} = 40$ Pa until they reach $p = 40$ Pa, above which the layer thickness decreases to 0.02 Pa (WBM simulations) or 0.012 (KDM simulations) in the uppermost layer. The

Table 1
Two-dimensional advection schemes for temperature and Ar mass mixing ratio in our simulations. The numbers 3, 77, 7 and 81 correspond to the advection schemes listed here in MITgcm code configuration. "•" means all the combinations we tested."☆" means the best combination we found in our simulations.

Adv. schemes	Ar, 3rd UW (3)	Ar, 2nd VL (77)	Ar, 7th OSMP (7)	Ar, SOM (81)
T, 3rd UW	•	•	•	•
T, 2nd VL	•	•	•	•
T, 7th OSMP	•	•	•	•
T, SOM	•	•	•	☆

Table 2
Properties of advection schemes used in our tests.

Adv. schemes	Full name	Accuracy	Flux limiter	Positive definite
UW	Upwind	3rd order	No	No
VL	Van Leer	2nd order	Yes	Yes
OSMP	One-step monotonicity preserving	7th order	Yes	No
SOM	Second-order moments	>4th order	Yes	Yes

top of the atmosphere then extends to 0.01 Pa or 0.006 Pa, corresponding to an altitude of ~90 km or ~100 km, in WBM or KDM simulations respectively. In order to properly parameterize the subgrid-scale processes in the PBL, we insert 12 physics layers in the first 80 Pa above the surface with layer thickness Δp_{phys} increasing from 0.5 Pa to 20 Pa as we move to higher altitudes. The typical horizontal grid resolution used for the Ashima/MIT Mars GCM simulations in this work is C18, equivalent to a 5.0° resolution on a latitude–longitude grid, and requires a time step of 240 s for WBM simulations or 120 s for KDM simulations to avoid CFL instabilities in both vertical and horizontal directions.

We assume Ar to be initially homogeneously distributed in the entire atmosphere with mmr $q_{Ar} = 0.0145$ everywhere, then begin our simulations at $L_s = 0°$ (northern spring equinox). This initial Ar mmr of 0.0145 (volume mixing ratio of 0.016), also used by Nelli et al. (2007), is chosen to be identical to the value measured by the Viking Lander 2 GCMS around $L_s = 134°$ (Owen et al., 1977). In fact, the choice of this initial value does not affect the model results because Ar is purely a passive tracer (thus its actual value does not affect model dynamics) and because the enhancement factor (EF) used for comparison with data and other models is based on the ratio of mmr *within* the model (see Appendix A). We perform tests of several advection schemes (Table 1) for temperature and Ar and seek combinations of schemes that best reproduce the observed polar Ar enhancement, with a focus on the peak southern polar winter EF, without sacrificing the quality of the large-scale dynamics.

The advection schemes in our tests include 3rd order upwind (UW, classic scheme without flux limiter), 2nd order Van Leer (VL) nonlinear flux limiter (low-order scheme with flux limiter), 7th-order one step method (OSMP) with monotonicity preserving limiter (high-order with flux limiter) and second-order-moment scheme (SOM, preserving high-order moments), among which the latter three are designed to reduce the numerical diffusion when the horizontal gradients of temperature or Ar mmr are large (such as at the polar front). The properties of these advection schemes are summarized in Table 2.

3. Results

We present Ashima/MIT Mars GCM results primarily using the wide-band radiative transfer model (WBM). While not the most accurate and flexible model available within the GCM, the WBM scheme is fast and yet captures the CO_2 and dust aerosol effects sufficiently well to simulate the mean climate; in addition, it is more convenient for performing inter-model comparisons as the same scheme was used to produce several published MarsWRF results (Richardson et al., 2007; Guo, 2009) and is similar to the band scheme used in the NASA Ames Mars GCM (Nelli et al., 2007). Additionally we present model results using the K-distribution radiative transfer model (KDM), which was recently used in data assimilation studies with MarsWRF (Lee et al., 2011).

In the following, we first describe the basic zonal mean climate simulated with the Ashima/MIT Mars GCM, including temperature and zonal wind (Section 3.1) and the CO_2 cycle (Section 3.2). In Section 3.3.1 we show the seasonal and latitudinal variation of non-condensable tracers (specifically argon), then go onto demonstrate the sensitivity of tracer transport to the choice of advection scheme (Section 3.3.2) and to atmospheric forcing (Section 3.3.3), and end with an assessment of the relative contribution to tracer transport by the mean flow and eddies (Section 3.3.4).

3.1. Basic dynamics

The Ashima/MIT Mars GCM produces a climate generally similar to other Mars GCMs and observational results (Haberle et al., 1993; Forget et al., 1999; Richardson et al., 2007; McCleese et al., 2010; Lee et al., 2011). Fig. 6 shows the seasonal variation of the time-averaged zonal mean temperature using the WBM and KDM radiative transfer schemes, and also a comparable plot using MCS observations. Overall the modeled temperature fields resemble the observed features in terms of the seasonal and spatial variations. It is apparent that the KDM scheme is more accurate in representing the observed temperature field from mid to low latitudes, at least in combination with our other physics parameterizations. Subtle differences include the WBM predicting a slightly cooler atmosphere between 100 Pa and 10 Pa and slightly warmer atmosphere above 10 Pa, while the KDM predicts less intensive heating at high latitudes during equinoxes. MCS observations from mid northern spring to mid northern summer show the density-scaled dust opacity (proportional to the dust mmr) to be enhanced between 10 Pa and 100 Pa (Heavens et al., 2011b), whereas our prescribed dust distribution decreases monotonically with height (see Section 2.2). We thus model cooler temperatures in those regions than are observed. In addition, the observed water cloud top extends above 10 Pa, higher than the dust top at most times, thus radiative cooling by the water cloud may produce cooler temperatures above 10 Pa, a process not captured by the Ashima/MIT Mars GCM as the present version does not include any water ice opacity. Finally, CO_2 cloud formed during polar night increases the aerosol opacity, the

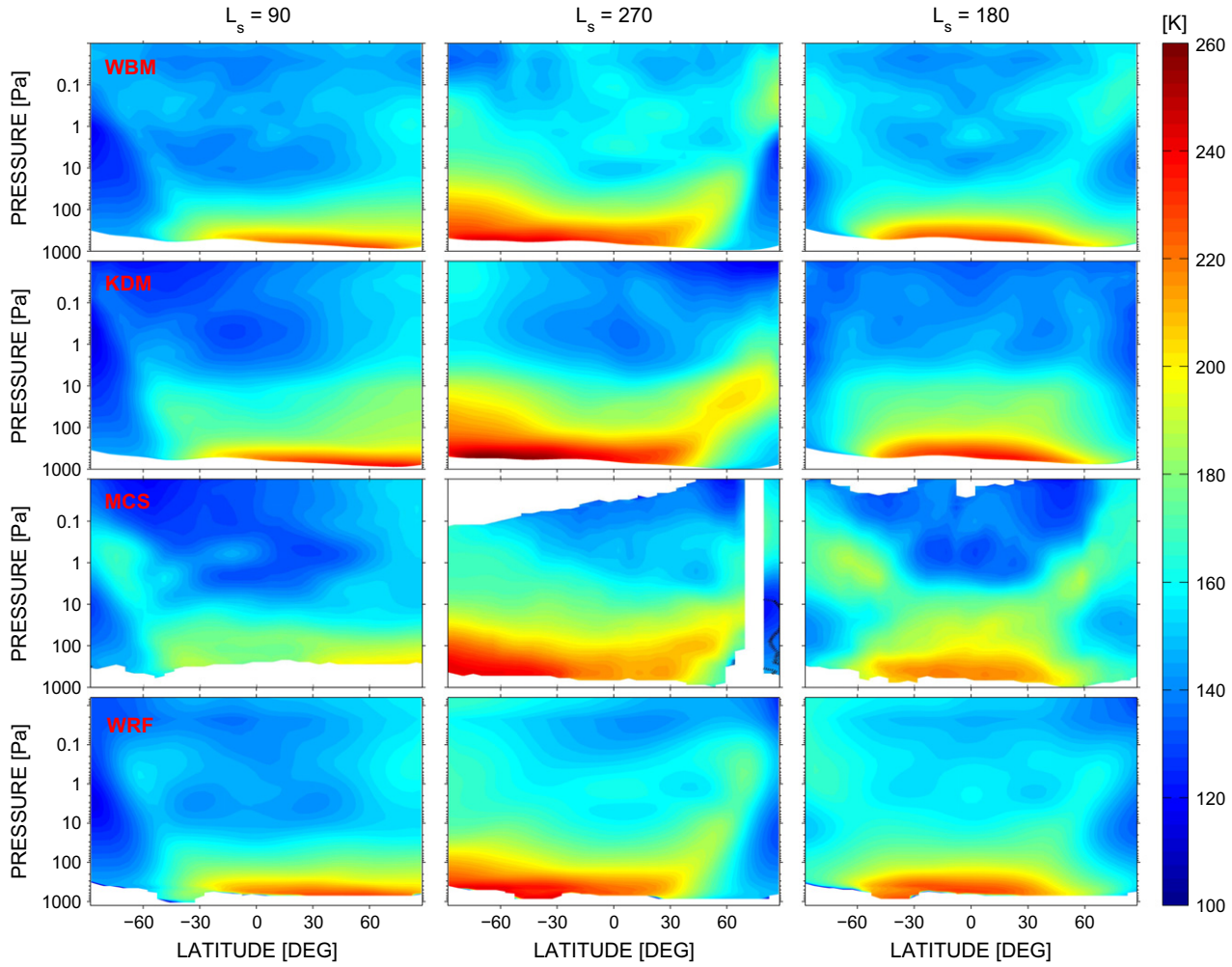

Fig. 6. Time averaged zonal mean temperatures for northern summer (L_s = 90°), winter (L_s = 270°), and autumn (L_s = 180°) for the Ashima/MIT Mars GCM using the WBM radiative transfer scheme (top row) and the KDM radiative transfer scheme (second row); for the MCS retrievals (third row); and, for the MarsWRF GCM using WBM radiation (bottom row). The MCS data have been averaged over 5° of L_s, the Ashima/MIT model 10° of L_s, and the WRF model 20° of L_s; in all cases centered on the L_s value indicated. The unit of temperature shading and the key is K.

representation of which would require a detailed CO_2 microphysics model (*e.g.*, Colaprete et al., 2008), which is again absent from this version of the GCM. The inclusion of a more realistic aerosol distribution is beyond the scope of this paper but will be included in future model development.

Interestingly, with the Ashima/MIT Mars GCM we are better able to capture the temperature inversion that occurs above both poles throughout the martian year (McCleese et al., 2008, 2010). According to the MCS temperature profile retrievals, this polar warming occurs above 2 Pa (roughly 40 km). Unlike MarsWRF and most other Mars GCMs, for which (as shown for MarsWRF) the warming is restricted away from the highest latitudes, we predict warming all the way to the pole in most seasons using the WBM scheme, and in some seasons with the KDM scheme. Compared to MarsWRF (Richardson et al., 2007), the reproduction of polar warming in the Ashima/MIT Mars GCM may be due to the slightly extended top of the atmosphere above 90 km, which allows greater adiabatic heating of the polar atmosphere by the descending branch of the fully developed Hadley cell circulation (Wilson, 1997; Forget et al., 1999). However, the reproduction of the observed polar warming for anything but the very highest of dust loadings is also likely to be dependent on the dynamical core. The only models to reproduce the observed warming to date are the Ashima/MIT Mars GCM (with its cube–sphere grid) and the Oxford Mars GCM (with its spectral dynamical core, Collins et al., 1996; Lewis et al., 1999), and have in common the lack of a "pole problem" thus do not require polar filtering (as do MarsWRF, the LMD Mars GCM, and the NASA Ames Mars GCM). While the Oxford spectral model (from 1999) predicted a polar warming about 50 K higher than the MCS observations during southern summer solstice, the Ashima/MIT Mars GCM overprediction is nearer 10–20 K at this season. The better match may be associated with dynamics, but it seems more likely that the lower optical depths in the more recent version of the MCD dust prescription (Montmessin et al., 2004) as compared to that used by the Oxford model at that time (Lewis et al., 1999; Forget et al., 1999) can explain this difference.

While there are no systematic observations of global winds, the zonal wind that would be in thermal wind balance with the MCS temperature retrievals has been calculated (Heavens et al., 2011a). For comparison, we show zonal mean zonal winds from the Ashima/MIT Mars GCM in Fig. 7. As the zonal mean temperatures are similar between the model and data, it should be no surprise that the derived winds are also similar. Common features at equinoxes are two eastward jets (80 ms^{-1}) at mid-latitudes along with a weak westward jet (10–20 ms^{-1}) at the equator. Common features during northern summer solstice are a single eastward jet in the southern hemisphere along with a broad westward jet

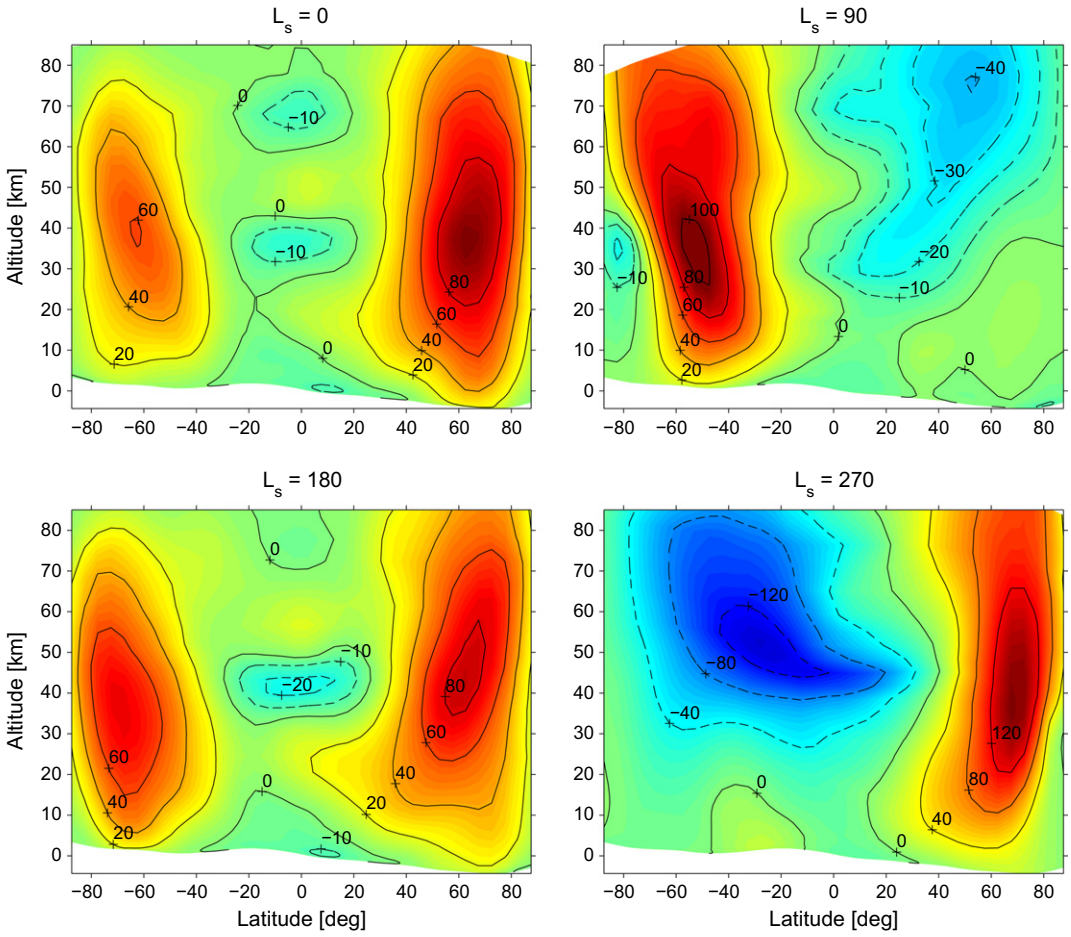

Fig. 7. Time averaged zonal mean zonal wind using the WBM radiative transfer scheme. The eastward wind is positive (solid lines) and the westward wind is negative (dashed lines). The unit of the contours is ms^{-1}.

spanning the equator and northern hemisphere, with this pattern reversed during northern winter solstice, though the winds are stronger during the latter season. The zonal wind decays with altitude above ~50 km for all four seasons, consistent with MCS data retrieved from thermal wind balance and with Oxford spectral model results (Lewis et al., 1999). The reduced zonal wind speed near the model top is largely caused by the Rayleigh drag, which is designed to damp upward propagating waves and limit artificial reflection in the top three model layers.

The Ashima/MIT Mars GCM produces an Eulerian mean meridional circulation with comparable pattern and strength to those of other Mars GCMs for all four seasons (Fig. 8). A pair of meridional overturning cells develop near the equator at both equinoxes with the stronger northern cell shifted 15–20° south of the equator. The downward slope of zonal mean topography from the southern to northern hemisphere is responsible for this asymmetric meridional circulation, whose effect has also been demonstrated in the GFDL Mars GCM (Richardson and Wilson, 2002a; Basu et al., 2004) and in a version of the MITgcm using Mars-like radiative–convective forcing (Zalucha et al., 2010). During both solstices, the mean meridional circulation is characterized as a single cross-equatorial meridional overturning cell and a pair of weak polar cells. During northern summer, a vestigial remnant of the southern summer cross-equatorial meridional overturning cell remains in the northern mid-latitudes. During southern summer, the single cross-equatorial cell completely dominates into the southern high latitudes. The strength of the southern summer cross-equatorial overturning cell is double to triple the strength of the northern summer cross-equatorial cell due to the much stronger solar forcing in this season and the aforementioned topographic asymmetry. It should also be noted that, in agreement with other GCMs, the cross-equatorial overturning cell is effectively pole-to-pole at altitudes above ~40–50 km. This degree of coupling between the lower and middle atmospheres may not be fully supported by MCS data, which show somewhat greater separation of the two circulation regions (Heavens et al., 2011a), with this disparity potentially being due to a difference between the modeled and actual vertical distribution of aerosols.

3.2. Tuning the Ashima/MIT Mars GCM's CO_2 cycle

Reproducing the observed CO_2 cycle is a key requirement for the study of argon mmr variations. In order to match observations, we tuned the seasonal CO_2 ice cap albedo and emissivity values following the procedure described by Guo et al. (2009). The values were tuned to produce a best fit match to observations for: (i) the daily-mean surface pressure measured at both Viking Lander sites (top panel of Fig. 9); and (ii) the ratio of ground CO_2 ice to total CO_2 (ice + atmosphere) mass estimated from GRS observations (bottom panel of Fig. 9). The resultant seasonal CO_2 ice cap properties used in this study are then: (north) albedo = 0.7 and emissivity = 0.5; (south) albedo = 0.5 and emissivity = 0.7. The model predicts as much as 26.5% of the atmospheric CO_2 mass condensing to form seasonal ice caps during a martian year. This value is slightly higher than the estimated 25% from GRS observations (Kelly et al., 2006; Titus and Colaprete, 2005; Prettyman and Titus, 2004) but lies within the range of NASA Ames and MarsWRF GCM predictions of 26–30% (Guo et al., 2009; Nelli et al., 2007). In fact,

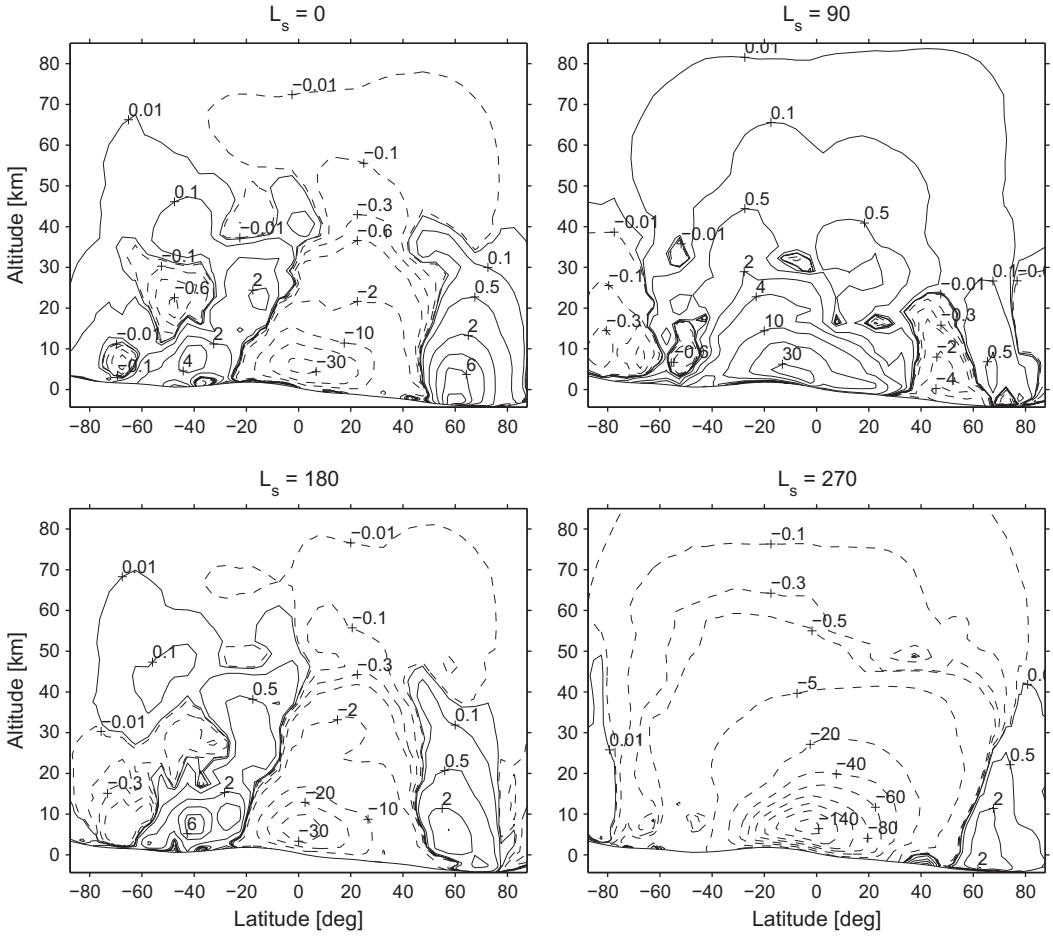

Fig. 8. Similar to Fig. 7 but for the mass streamfunction. The positive flow is counterclockwise (solid lines) and the negative flow is clockwise (dashed lines). The unit of the contours is 10^8 kg s^{-1}.

tests with the CO_2 mass ratio adjusted to 26% or 30% by increasing or decreasing the total initial CO_2 mass in the Ashima/MIT Mars GCM suggest the modeled Ar enrichment/depletion is insensitive to these changes. Ideally one would also match the observed total ground CO_2 ice mass, however all current Mars GCMs predict ground CO_2 ice mass to be higher than observations by 16–25% if they are to match the Viking Lander pressure curves (Guo et al., 2009; Haberle et al., 2008; Nelli et al., 2007). It should be possible to reproduce every aspect of the seasonal CO_2 cycle by simultaneously tuning every physics parameter that affects the atmospheric CO_2 budget (including surface ice albedo and emissivity, subsurface variations in conductivity, and the distribution and variability of atmospheric aerosols that effect surface radiative heating – see *e.g.* Guo et al., 2009; Kahre et al., 2010). However, this would be an extremely time-consuming and iterative process (as well as aspects like the microphysics and radiative properties of CO_2 ice particle aerosols remaining incompletely understood). Determination of the optimal configuration is beyond the scope of this paper and in any case is not needed for this study so long as the cycle of atmospheric mass is roughly correct, which we have gauged from comparison with the Viking Lander pressures (Fig. 9a).

3.3. Seasonal variation of polar argon abundance

3.3.1. Ar enhancement

The calculation of the Ar enhancement factor (EF) follows Sprague et al. (2007) and is described in detail in Appendix A. If EF is greater/smaller than unity, then Ar is respectively enhanced/depleted relative to the column-averaged mmr modeled at Viking Lander 2 at $L_s = 135°$. Using the KDM radiative transfer scheme with the SOM temperature and tracer advection schemes, the Ashima/MIT Mars GCM produces amounts and timings of Ar enhancement that come close to matching MY26 GRS observations for most of the year, but underpredict EF from southern mid-autumn to mid-winter, with peak values of roughly EF = 4.75 predicted compared to 6 observed (Fig. 1). Despite not matching the observations, the Ashima/MIT Mars GCM peak value remains higher by at least 50% than all other model simulations published to date. Fig. 1 shows the seasonal variation of Ar enhancement factors at the south and north poles for our best case WBM and KDM simulations, along with GRS observations and MarsWRF, LMD, and NASA Ames Mars GCM results. The south polar Ar mmr has a moderate increase during the southern autumnal equinox then builds up rapidly, in response to CO_2 condensation, resulting in EF values that exceed unity between $L_s = 0°$ and $L_s = 180°$, and reach peak values of roughly 3.5 near $L_s = 120°$ in the WBM simulation and 4.75 near $L_s = 110°$ in the KDM simulation. The south polar Ar mmr decreases through late northern summer and autumn equinox, after which EF in general remains below unity, as a consequence of Ar dilution in the south polar region. EF reaches a minimum value of 0.4–0.6 during southern summer solstice when CO_2 condensation ceases and all surface CO_2 ice sublimates at the south pole. Ar mmr return to their initial values during northern spring, and this seasonal cycle roughly repeats from year to year.

At the north pole, Ar abundance has significantly weaker variation with seasons. It stays close to the homogeneous mixing ratio

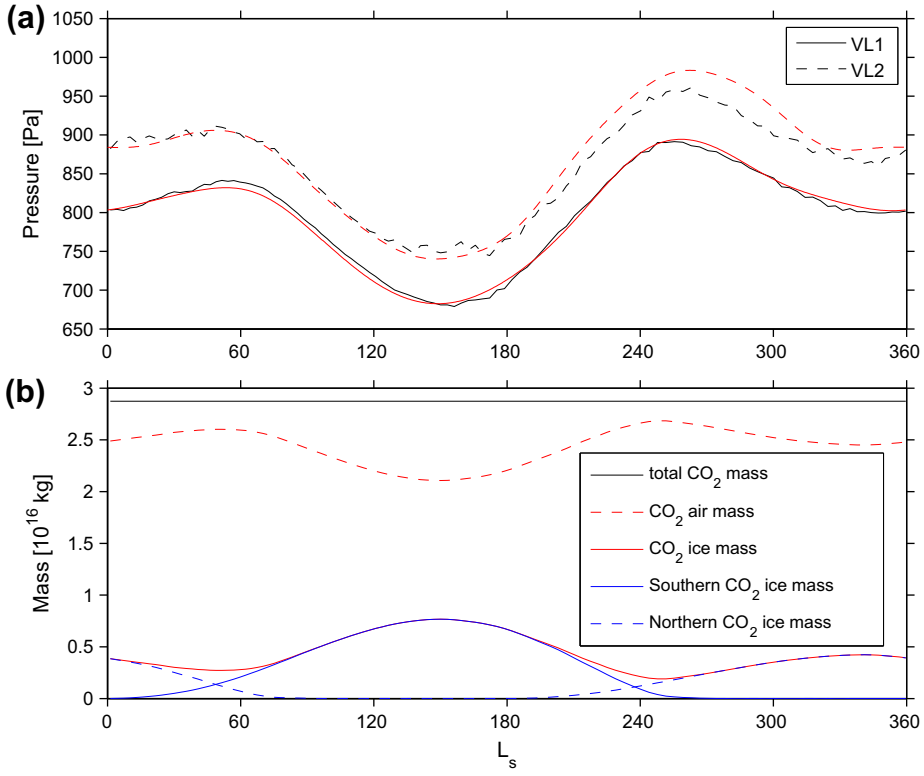

Fig. 9. CO_2 cycle in the martian atmosphere. Panel (a) shows the simulated pressure curves (black) comparing to the best fits of the observed (red) at Viking Lander 1 site (solid curves) and Viking Lander 2 site (dashed curve). Panel (b) shows the total CO_2 mass (solid black line), CO_2 air mass (dashed red line), total CO_2 ice mass (solid red line) and the hemispheric CO_2 ice mass (soild and dashed blue lines).

for much of the time, and the north polar EF only reaches roughly 2 briefly during northern winter. Our modeled temporal variation of Ar enhancement does not capture an apparent high-frequency oscillation in EF with a period of $\Delta L_s = 30°$ seen in the GRS-derived values. However, the amplitude of this oscillation is comparable to the GRS derived error bars, so the robustness of this feature in the real atmosphere is unclear.

Fig. 10 shows the temporal variation of zonally averaged Ar mmr and mass density using the KDM radiative transfer scheme and SOM temperature and tracer advection schemes. The Ar abundances are largest near the poles and decrease gradually towards the equator, with Ar at the south pole experiencing an enhancement several times higher than its counterpart at the north pole. The Ar EF outside of the polar regions is also comparable to the GRS observations at other high latitudes. The mass density and mmr ratios show the seasonal variation of Ar and demonstrate the clearly asymmetric distribution between the south and north poles during winter and summer. Such dichotomy arises from the significant differences in the effective "source strength" (*i.e.*, intensity of CO_2 condensation) affecting the enhancement of Ar mmr in the south versus the north. There is also very clear pole-to-pole transport in late winter and early spring in each hemisphere as the winter/spring seasonal cap sublimes. Compared to the GRS data, the variation of our modeled Ar EF at low latitudes in the southern hemisphere and over the entire northern hemisphere appears to be too smooth. However, this may be due to noise in the GRS observations, though potential causes of this have not been determined to date.

As in most other Mars GCMs, our model predicts the north polar Ar variation largely within the error bars of the observations. However, the Ashima/MIT Mars GCM predicts the seasonal variation of south polar Ar abundance significantly better than other comparable Mars GCMs (Fig. 1). Nelli et al. (2007) performed the first work on non-condensable tracer transport in the martian atmosphere using the NASA Ames Mars GCM. They were able to reproduce the temporal variation of the observed Ar mmr but with magnitudes that were about a factor of 2.5 too small. Guo (2009) produced even less Ar enhancement using MarsWRF despite their careful tuning of the CO_2 cycle (discussed further in Section 3.2) which one might expect to improve the quality of polar dynamics overall. In fact, their modeled Ar enhancement factor at the south pole was about a factor of 3 smaller than that observed (Guo, 2009). Lefèvre and Forget (2009) were able to produce a peak Ar EF with the LMD Mars GCM that was a little higher than that of Ames, but still about a factor of 2 too small compared to observations (see also Appendix A). In their model, the Ar enhancement factor has an initial peak of roughly 2.5 near $L_s = 60°$ then a primary peak of roughly 3 near $L_s = 150°$. Their simulated temporal variation of Ar enhancement also has several mismatches with observations in southern autumn and winter. The trend in EF between $L_s = 60°$ and roughly $L_s = 150°$ is opposite to that observed (with a modeled local minimum at $L_s = 115°$), and their maximum Ar EF (at $L_s = 150°$) is significantly time-lagged in comparison to the observed peak at $L_s = 100$–$120°$. In fact, Nelli et al. (2007) showed that outflow of Ar from the south polar region reaches its peak at $L_s = 150°$ based on the data derived from GRS observations, so a maximum in predicted polar Ar enhancement at this time of year is rather difficult to understand.

In short, the models used to date significantly underestimate the peak and potentially also the seasonal evolution of EF over the southern pole in southern autumn and winter.

3.3.2. Tracer advection

It is likely that the use of different dynamical cores (*e.g.*, finite volume vs. finite difference) can greatly affect tracer transport, as demonstrated by the inter-model comparisons shown above,

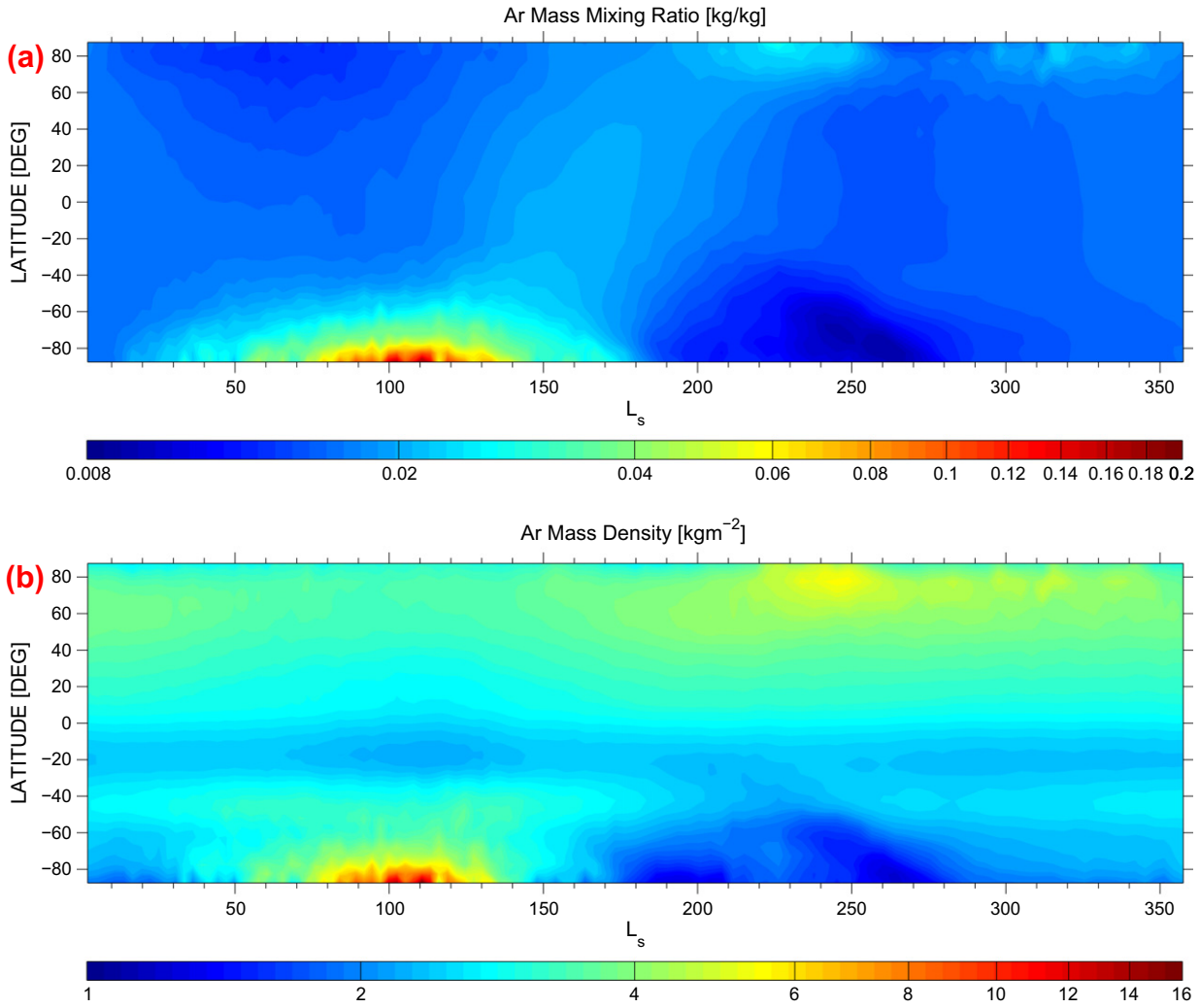

Fig. 10. Seasonal variation of the zonal-mean Ar column mmr (a) and Ar column mass density (b). Note that the column mmr can be used to calculate the EF by scaling any value shown by the modeled value at 48°N and at $L_s = 135°$ (0.017).

especially considering that the Ashima/MIT Mars GCM (using the WBM radiative transfer scheme) and MarsWRF share the same physics package. However, the numerical treatment of tracer advection within each GCM can also greatly impact the temporal variation of tracer fields. Both effects have generally been ignored in GCM studies of the martian atmosphere, likely because of lack of constraining observations and also because of concerns that aerosol forcing uncertainty dominates model error. The importance of transport representation to Earth atmosphere/ocean studies has long been known (Hourdin and Armengaud, 1999; Read et al., 2000; Gregory and West, 2002; Iselin et al., 2005; Hill et al., 2012). We thus performed sensitivity studies for tracer transport in the Ashima/MIT Mars GCM using various tracer advection schemes in conjunction with the WBM radiative transfer scheme. In addition, we tested several temperature advection schemes that affect the circulation and CO_2 condensation, and consequently the Ar mmr. Spatial and temporal variation of tracers in GCMs are governed by their continuity equations, in which advection schemes describe the movement of tracers between grid boxes (or grid points). Tracer schemes vary in their properties and behavior. A low-order linear scheme in general tends to produce grid-scale smoothing (numerically diffusive), averaging dynamic variables in certain areas with consequent loss of local information. In a system where eddy activities dominate tracer transport, one would prefer to use a scheme with a flux limiter to keep the tracer fields local, meaning the smoothing effect of advection schemes should not exceed the eddy transport rates.

Fig. 11 shows the temporal variation of EF at the south pole (left column) and the north pole (right column) for various transport schemes used in the Ashima/MIT Mars GCM. Note that different schemes have been applied to the tracer (Ar) and temperature fields separately. It is obvious that the advection schemes only affect tracer transport during the time when CO_2 condensation leads to dramatic changes in the local tracer mixing ratio. Various combinations of tracer advection schemes and temperature advection schemes can lead to changes of EF by as much as 40% at the southern winter pole and 30% at the northern winter pole. Among all the combinations, the VL temperature advection with OSMP tracer advection scheme yields the smallest Ar enhancement factors at both poles as seen in the second row of Fig. 11, where the black lines show a maximum enhancement factor of 2.8 at the south pole (left panel) and 1.8 at the north pole (right panel). The largest Ar enhancement factors, however, are produced by a different combination depending on the pole: at the south pole, the SOM scheme for both temperature and tracer advection, giving EF = 4 (as shown by the green line in the bottom left panel), and at the north pole, the upwind temperature advection scheme and SOM tracer advection scheme, giving EF = 2.25 (as shown by the green line in the top right panel).

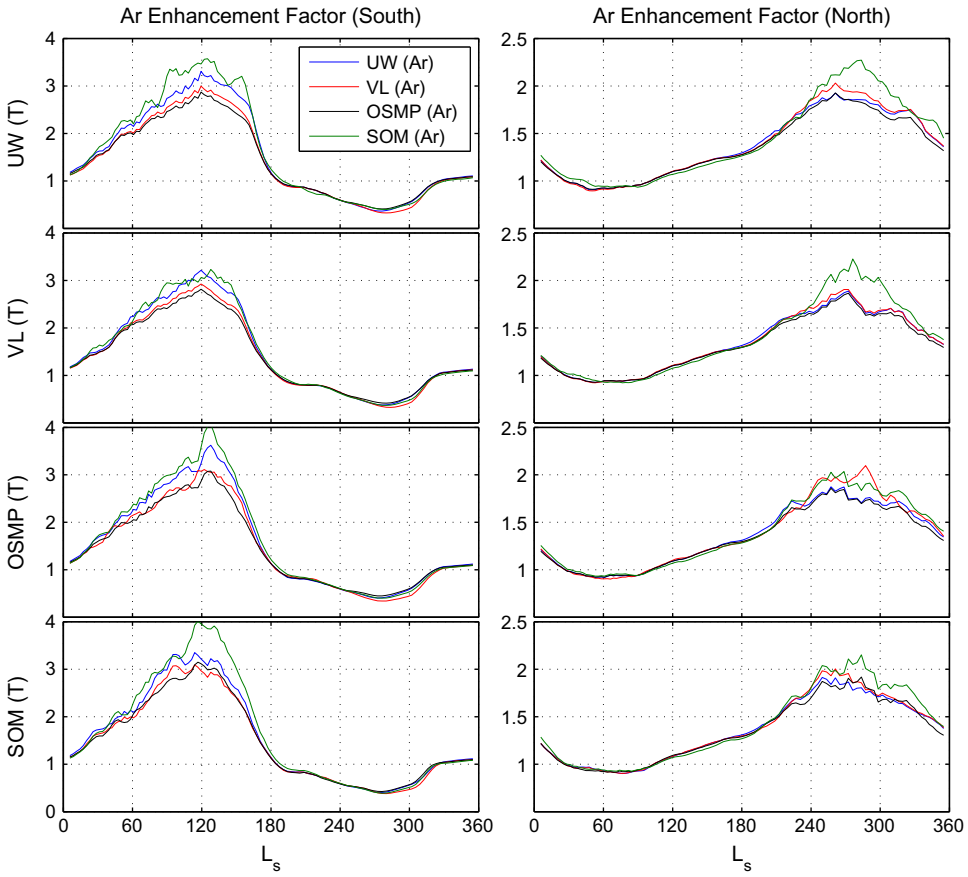

Fig. 11. Seasonal variation of EF at the south pole (left column) and north pole (right column) as a result of different tracer and temperature advection schemes. The rows from top down show the EF with fixed temperature advection schemes including 3rd-order UW, 2nd-order VL, 7th-order OSMP and SOM. For each temperature advection scheme there are four different tracer advection schemes: 3rd-order UW (blue line), 2nd-order VL (red line), 7th-order OSMP (black line) and SOM (green line) that is also shown as the black lines but without time average in Fig. 1. The EF values are all averaged over a period of $L_s = 10°$.

There is a clean trend in south-polar Ar enrichment by varying tracer advection schemes while fixing the temperature advection scheme: for each choice of fixed temperature advection shceme, the SOM tracer advection scheme produces the largest enhancement factor, followed by the UW scheme, the VL scheme and OSMP scheme. Such a trend cannot be seen at the north pole, where most of the tracer advection schemes behave quite similarly except that the SOM tracer advection scheme generally produces larger enhancement factors. Fig. 12 demonstrates how the tracer advection scheme can alter the tracer field by comparing the zonal mean Ar mmr averaged over 45° of L_s during southern winter. Despite the dynamics in the two cases being identical (as they share the same temperature advection scheme: the SOM in this case), the SOM tracer advection scheme produces higher concentration of Ar poleward of 60°S and between 1 and 20 Pa than the VL scheme does. The cause of the difference is that the SOM advection scheme numerically reduces the equatorward leak of Ar, which leads to small Ar mmr over broader vertical extent at low-to-mid latitudes in the southern hemisphere as well as the majority of the northern hemisphere.

Temperature advection schemes have an impact on polar Ar enrichment too. For a fixed tracer advection scheme among the UW, VL and OSMP schemes, any temperature advection schemes generally produces a maximum EF of around 3 at the southern winter pole and 2 at the northern winter pole. However, varying the temperature advection schemes can lead to a difference of EF of up to about 35% when we select the SOM tracer advection scheme. At the southern winter pole, both OSMP and SOM temperature advection schemes produce a maximum EF of 4, with the latter maintaining this maximum value for a longer duration (about 30° of L_s). The UW temperature advection scheme reduces the maximum value to 3.5 but the Ar enrichment shows a flatter and wider peak in contrast to the sharp peak centered at $L_s = 120°$ in other advection schemes. The VL temperature advection scheme produces the smallest EF when combined with the SOM tracer advection. Indeed, the temporal variation of Ar enrichment is least sensitive to the selection of tracer advection schemes under this temperature advection scheme. At the northern winter pole, the choice of temperature advection scheme has the opposite effect to that at the southern winter pole. The UW and VL schemes produce a maximum EF of 2.25 sharply peaked near $L_s = 270°$ while the other two schemes produces smaller and noisier EF. The dichotomy of the temperature advection scheme effect between the two winter poles is seemingly caused by the difference in atmospheric heating, which is stronger during southern summer due to the increased dust opacity.

Our study of the sensitivity of tracer transport to choice of advection schemes suggests that certain combinations of temperature and tracer advection schemes definitely improve the GCM's representation of polar Ar enrichment. Numerical treatment of both temperature and tracer transport can affect the temporal variation of the polar Ar EF, due to modification of the atmospheric circulation, due to modifying the amount of CO_2 condensation, and due to directly modifying Ar transport. Fig. 13 (top row vs. middle row) shows the effect of temperature advection on the zonal mean CO_2 condensation and tracer distribution during

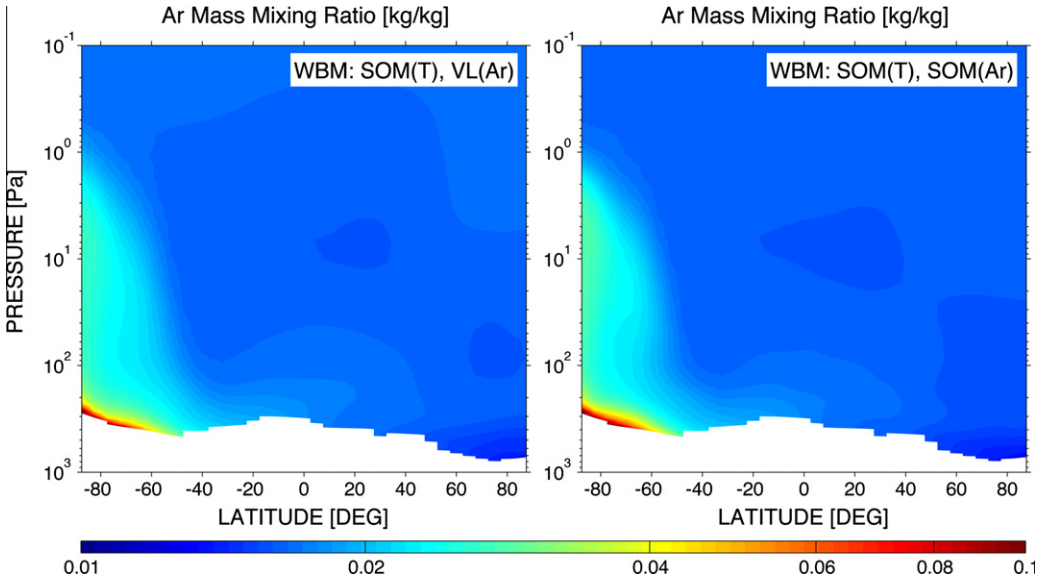

Fig. 12. Comparison of Ar mmr between the VL and SOM tracer advection schemes with fixed SOM temperature advection scheme. The zonal mean mmr is time averaged from $L_s = 90°$ to $L_s = 135°$.

southern winter. The atmospheric CO_2 condensation here indicates where the Ar mmr is expected to increase due to this process. Both SOM and VL temperature advection schemes produce a maximum CO_2 condensation between 50 Pa and 100 Pa where a local maximum of Ar mmr might then also be expected (middle and top right panels). However, the actual Ar mmr has a minimum, suggesting that Ar mmr is either transported vertically or mixed horizontally away from this region (middle and top left panels). The former appears to be the case in our simulations as the Ar mmr has a maximum above 10 Pa (also see discussion in Section 3.3.4). In the region from 40°S towards the north pole where CO_2 condensation is absent, the Ar mmr is ~1% smaller when using the SOM temperature advection scheme. We should note that this small difference could cause a much larger difference in polar Ar mmr as the area of the polar region (defined as poleward of 70°) is only 7% of the rest of the planet. Therefore the importance of the temperature advection schemes on dynamical transport of Ar cannot be underestimated. This further leads to some difficulty in isolating the relative importance of temperature and tracer advection representation. Nonetheless, our study suggests the effect of temperature and tracer advection schemes on tracer transport must both be taken into account for understanding tracer evolution.

3.3.3. The effect of radiative heating representation on Ar distribution

Besides the effect of advection schemes on tracer distribution, another important aspect we must consider is the net radiative heating that drives both the circulation and the CO_2 cycle. Fig. 13 (middle row vs. bottom row) shows that the KDM radiative transfer scheme produces zonal mean profiles of CO_2 condensation and polar Ar distribution that look quite different to those produced by the WBM scheme, although a close correlation between CO_2 condensation and Ar enhancement is evident using both radiative transfer models. Using the KDM scheme, CO_2 condensation poleward of 80°S has a larger vertical extent than using the WBM scheme, and (unlike the WBM scheme) CO_2 condensation also occurs in a thicker layer at low altitudes between 60°S and 90°S. Despite this, the annual variations of total CO_2 ice using the KDM and WBM schemes are nearly identical. The Ar mmr in both cases is largest near the surface and rapidly decreases with altitude. The notable difference between the two cases is that the KDM scheme produces a local maximum of Ar mmr between 1 Pa and 2 Pa, much higher than the local maximum at 10 Pa using the WBM scheme.

Neither the WBM nor the KDM scheme allows the Ashima/MIT Mars GCM to replicate the vertical distribution of polar Ar mmr similar to that predicted by the NASA Ames GCM. Nelli et al. (2007) produced a local maximum of CO_2 condensation near 50 Pa where the Ar mmr was greatly enhanced over the southern winter pole. They found that excessive Ar transported out of the polar region by eddies at this pressure level resulted in a small EF of 3. Nelli et al. (2007) further speculated that larger EF could be produced if all CO_2 condensation occurred near the surface where eddy mixing was weak. We find this level of local maximum CO_2 condensation (50 Pa) in our model to be consistent with theirs. However, all our model results show that the polar Ar mmr has the highest concentration near the surface. Therefore, Nelli et al.'s (2007) speculation that CO_2 condensation must occur near the surface does not appear to be a necessary condition for large EF values. Colaprete et al. (2008) showed alternatively that greater Ar enhancement could be achieved if Ar were convectively lifted to a region above 10 Pa where polar confinement was strongest. Despite the different vertical distributions of Ar mmr, these studies all suggest that a higher Ar EF could be achieved if peak Ar mmr were out of reach of strong eddy mixing. That is, Ar mmr needs to be localized either near the surface, or at a high altitude, or in both regions. Our model's ability to capture both scenarios possibly explains the generally higher Ar EF compared to that in the NASA Ames GCM. Furthermore, the dissociation between the maximum Ar mmr and the maximum CO_2 condensation in our model suggests rapid redistribution of Ar mmr through dynamical processes, which are discussed further in the following section.

3.3.4. Mean and eddy transport

The temporal and spatial variation of non-condensable tracer mass is regulated by dynamical transport. If each atmospheric column were isolated, the Ar mmr would vary only due to the reduction/increase in total column CO_2 mass (*i.e.* the increase/reduction of the numerator in the mmr calculation as CO_2 sublimes/condenses, respectively). However, at the winter pole, sufficient CO_2 condenses that additional atmosphere is dynamically "pulled in" to the pole due to the reduction in surface pressure. The most idealized way of examining the amount of extra Ar mass thus brought

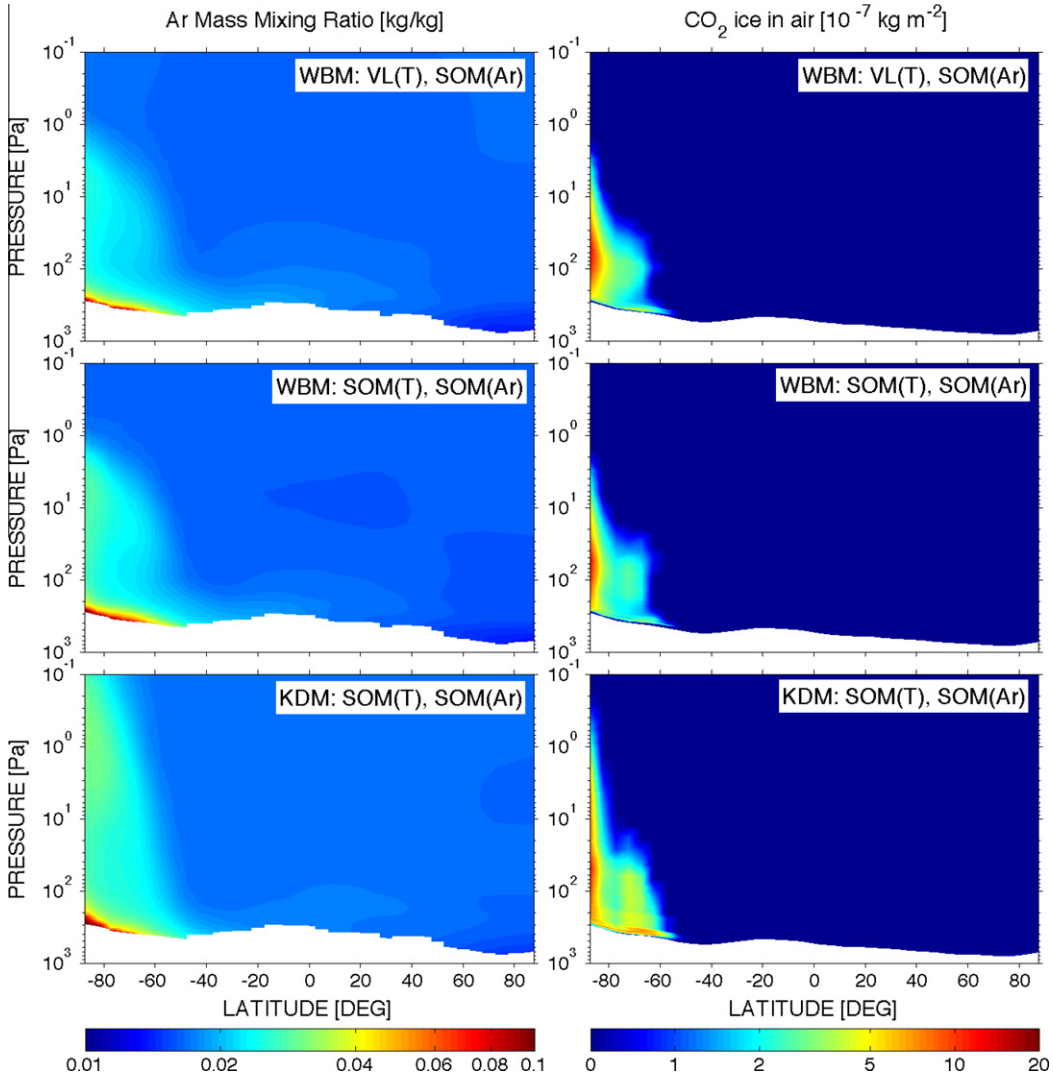

Fig. 13. Comparison of Ar mmr and CO_2 ice in air between the VL and SOM temperature advection schemes with fixed SOM tracer advection scheme. The top two rows show the results with the WBM radiative transfer scheme and the bottom row shows the result with the KDM radiative transfer scheme. The zonal mean mmr is time averaged from $L_s = 90°$ to $L_s = 135°$.

into the condensing polar region follows Sprague et al. (2004). If we assume that the only inflow of "fresh" (extra polar) atmosphere is that amount necessary to perfectly balance condensational loss of CO_2 to the ice cap, and that there is thus no outflow, then the inflow mass is equal to that needed to yield latent heating to balance infrared cooling to space from the winter polar column. The results of this idealized model are shown by Sprague et al. (2004) using a simplified energy balance model and by Nelli et al. (2007) and Guo (2009) using a GCM to calculate the polar energy balance (and hence require latent heating). The results are very similar due to the effectively negligible heat carrying capacity of the atmosphere. Using this simplified "non-transport" model (which is not completely a valid name for the scheme as it allows transport in but not out), they found that polar Ar mass continuously accumulates between $L_s = 0°$ and $L_s = 180°$ with dilution beginning thereafter when sunlight returns to the southern pole. The resulting EF reaches peak values of 9–10 at $L_s = 180°$ and is restored to unity when the seasonal ice cap disappears at summer solstice. Comparing with observations, the much larger EF values and greatly delayed peak produced by this "non-transport" scenario indicate the existence of dynamical transport processes that leak Ar out of the polar vortex during southern winter.

To determine how dynamical transport affects the Ar distribution, we inspect the time evolution, mean and eddy fluxes of Ar mass. First we define some diagnostics quantities that depict the tracer transport over a martian year. The rate of change of zonal mean Ar mass density, which provides the total flux transported by the mean meridional circulation (thermally direction circulation), condensation flow (a slow meridional flow driven by the geopotential contrast induced by CO_2 condensation) and eddies, is defined as

$$\frac{\partial M_q}{\partial t} = \overline{\frac{\partial}{\partial t}\left[\int_0^{p_s} q\frac{dp}{g}\right]} \tag{16}$$

where p_s is the surface pressure and q is the Ar mmr. In the above equation, the tracer mass density is vertically integrated and zonally averaged (denoted by []) and then differentiated between two consecutive model output snapshots. We average the rate of change of tracer mass density over 10° of L_s to eliminate any short period oscillations. To better illustrate the role of mean and eddy transport on tracers, we adopt similar mean and eddy diagnostics to Nelli et al. (2007) and Peixoto and Oort (1992),

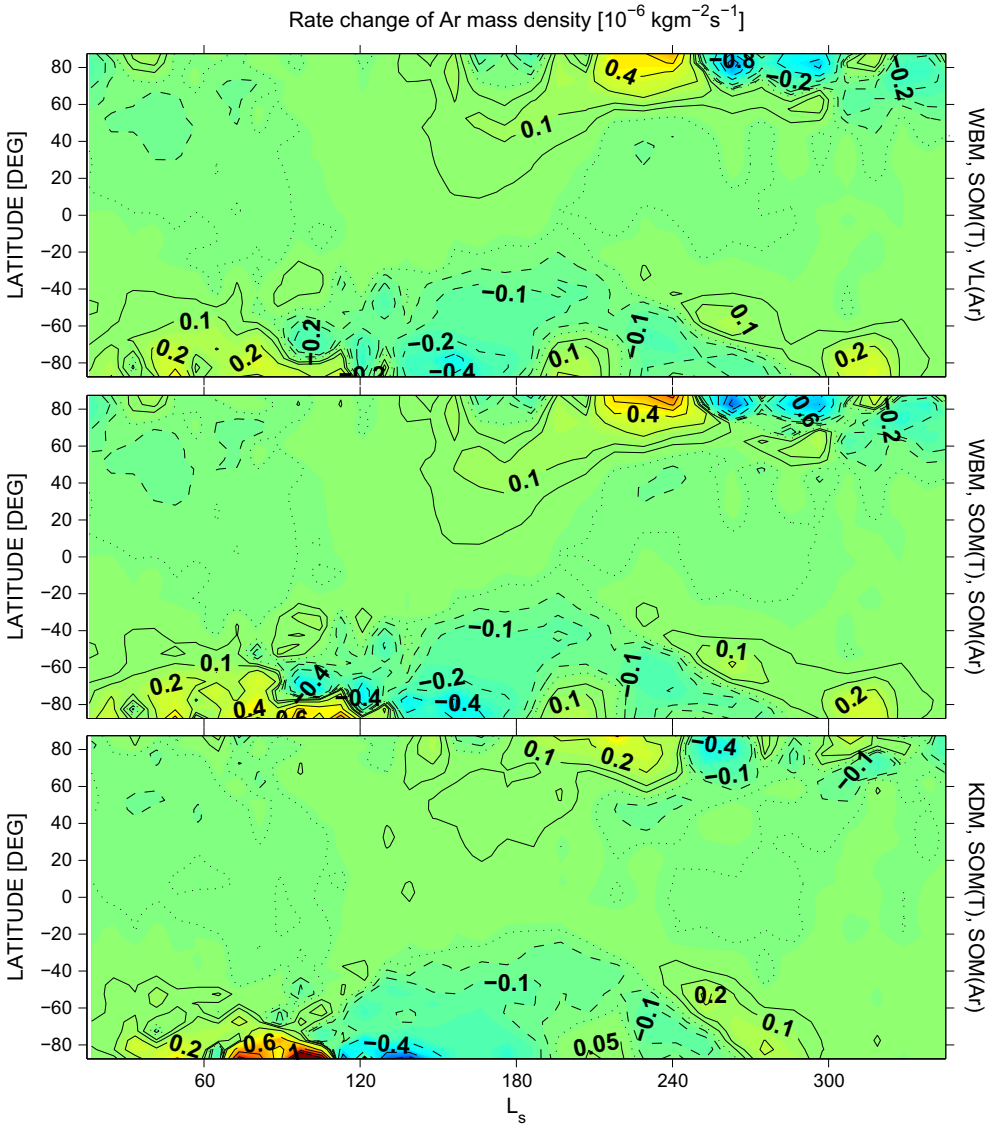

Fig. 14. Comparison of the rate change of the Ar mass density for the WBM simulations with the SOM temperature and VL tracer advection schemes (top row), the WBM simulations with both SOM temperature and tracer advection schemes (center row) and the KDM simulations with both SOM temperature and tracer advection schemes (bottom row). The Ar mass density is vertical integrated and zonally averaged. The rate change is time averaged over 10° of the solar longitude. The solid lines with reddish color are the increase rate and the dashed lines with bluish color are the decrease rate. The dotted lines are the zero rates.

$$[\overline{v}\overline{q}]\frac{\Delta p}{g} = [\bar{v}][\bar{q}]\frac{\Delta p}{g} + [\bar{v}^*\bar{q}^*] + [\overline{v'q'}])\frac{\Delta p}{g} \tag{17}$$

where Δp is the layer thickness in pressure. The term on the left $[\overline{v}\overline{q}]$ is the total meridional transport of tracer that is temporally and zonally averaged. On the right-hand side, the first term is the zonal-mean tracer transport, the second term is the tracer transported by stationary eddies (deviation from zonal mean that is denoted by *) and the third term is the transport by transient eddies (deviation from time average that is denoted by $'$). For simplicity, we only consider the total effect of stationary and transient eddies when discussing eddy fluxes.

It is worth mentioning that the decomposition in Eq. (17) is arguably inaccurate for the martian atmosphere. In η coordinates, where the pressure levels intersect with topography, the zonal mean of dynamic variables are averaged either into the topography or over a limited number of points above topography, which violates the assumption of zonally symmetric flow for such decomposition (Peixoto and Oort, 1992). Terrain following coordinates (such as the σ coordinates) are also plagued by the large variation of topography in the zonal direction (*e.g.*, the Hellas basin and Olympus mons), which causes the σ levels to vary by over a scale height near the surface. The decomposition in Eq. (17) does provide an accurate quantitative evaluation of tracer transport above the level of maximum topography; however, if we were to vertically integrate results over the entire column we would include the region below this level, for which Eq. (17) produces increasingly inaccurate results (since as we descend in height below this level we are increasingly unable to generate a valid zonal average due to the presence of topography). We therefore do not perform or show vertical integrations of the mean or eddy fluxes (and thus do not compare with those shown in Nelli et al. (2007)).

The hemisphere-to-hemisphere redistribution of Ar mass is the dominant process that leads to the seasonal polar enrichment and depletion of Ar. Fig. 14 shows the rate of change of column integrated zonal mean Ar mass density. At mid-to-high latitudes in southern hemisphere, more specifically 75°S–90°S, Ar mass starts to accumulate at spring equinox and this continues until about

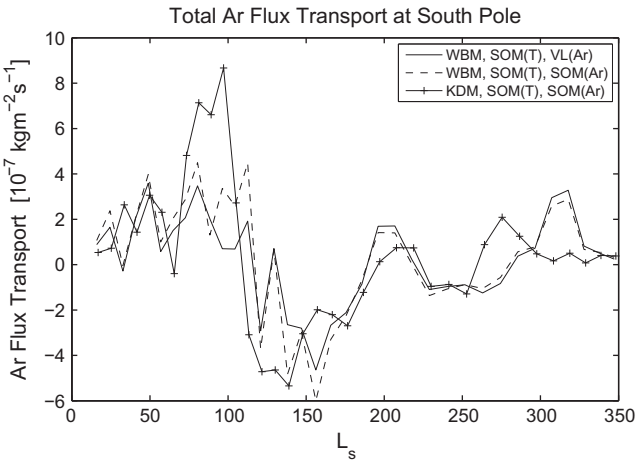

Fig. 15. Comparison of net Ar flux in the south polar region for the WBM simulations with the SOM temperature and VL tracer advection schemes, the WBM simulations with both SOM temperature and tracer advection schemes and the KDM simulations with both SOM temperature and tracer advection schemes. The net flux is integrated in a 15-degree latitudinal bin starting from the south pole.

$L_s = 120°$, after which Ar mass decreases rapidly between $L_s = 120°$ and $L_s = 150°$, despite the fact that CO_2 condensation reaches its maximum in the southern hemisphere during this period (Fig. 9b). Moderate oscillations with a period of ~30° of L_s occur during early autumn and late southern summer. In the northern hemisphere, the change of Ar mass is anti-correlated with its counterpart in the southern hemisphere. We estimated the total Ar mass and its rate of change for the region poleward of 75° in both hemispheres. During southern winter, the decrease of Ar mass at the north pole only accounts for about 15–20% of the increase at the south polar region in the WBM simulations, and even less in the KDM simulations. The rest of the Ar comes from mid-to-low latitudes in the northern hemisphere. During northern winter, however, the decrease of Ar mass at the south pole accounts for more than 50% of the Ar mass increase at the north pole. The latter suggests a stronger pole-to-pole transport of Ar mass, possibly due to the stronger cross-equatorial mean overturning circulation in the southern summer season. Regional exchanges of Ar mass can also be seen near 70° in both hemispheres, which leads to higher Ar mass transport poleward and lower mass transport equatorward.

Different tracer advection schemes and radiative transfer schemes affect the total tracer fluxes in detail, but not their overall pattern. First we compare two cases where temperature advection is performed using the SOM scheme while tracer advection uses either the VL (upper panel in Fig. 14) or the SOM (middle panel in Fig. 14) schemes. The difference in rate of change of Ar mass between the two tracer advection schemes is visible throughout a martian year and is more pronounced at the southern winter pole. Using the SOM scheme, both the increase and decrease in Ar mass

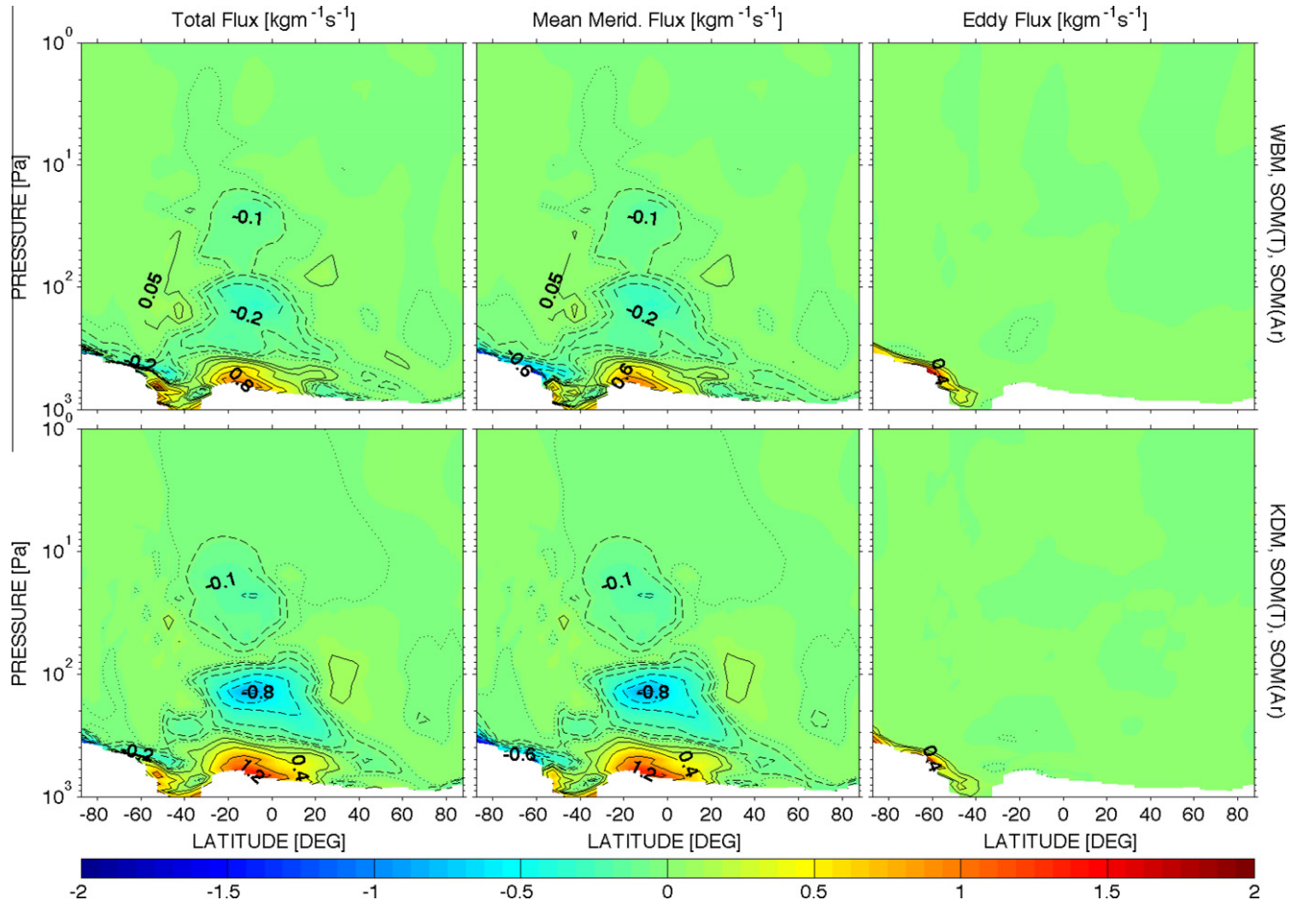

Fig. 16. Comparison of the total (left column), advective (center column) and eddy fluxes (right column) of Ar for the WBM simulations with both SOM temperature and tracer advection schemes (top row) and the KDM simulations with both SOM temperature and tracer advection schemes (bottom row). The zonal mean fluxes are time averaged over 60° of the solar longitude centered at $L_s = 90°$ (southern winter). The solid lines with reddish color are the northward fluxes and the dashed lines with bluish color are the southward fluxes. The dotted lines are the zero fluxes.

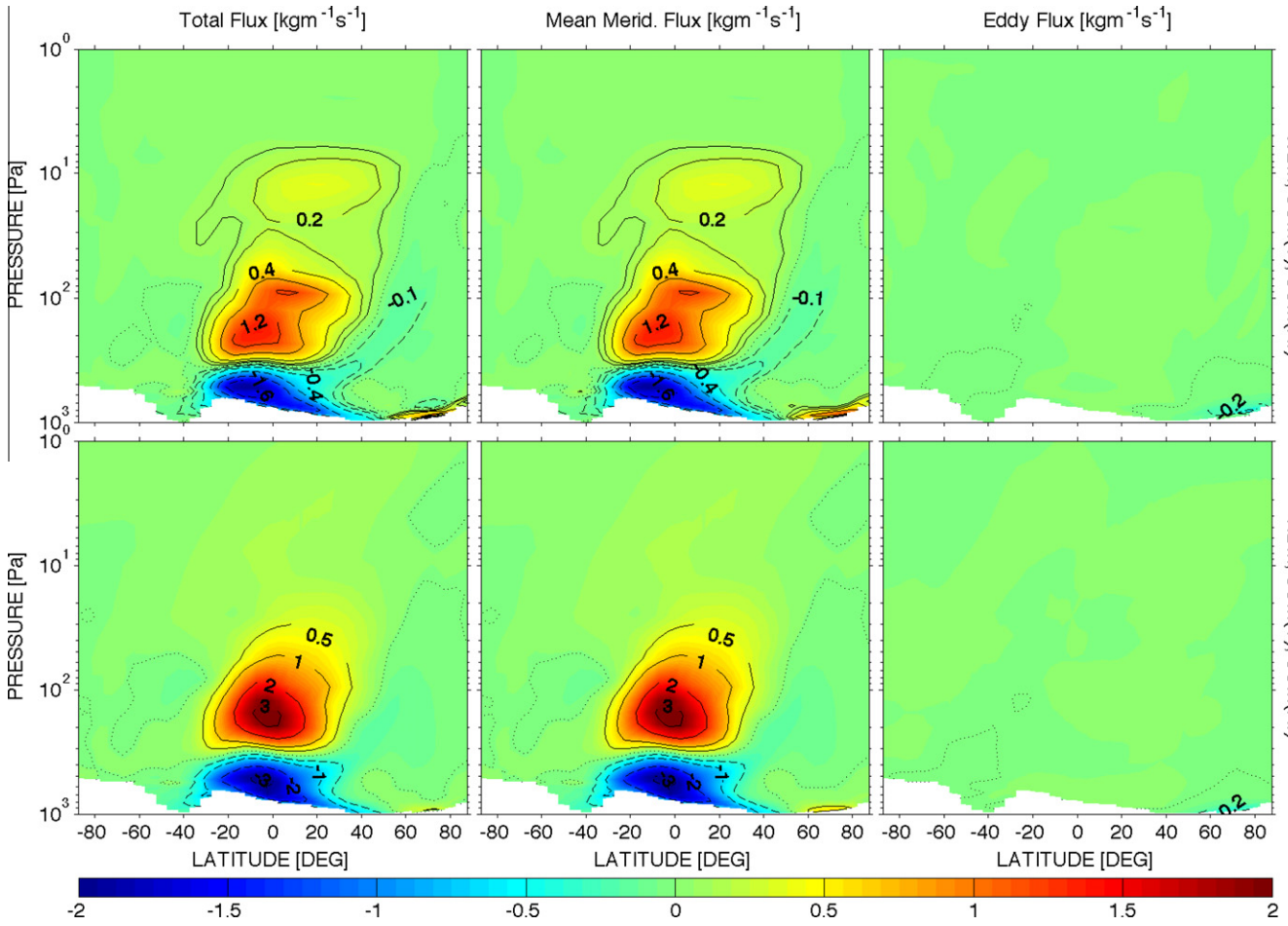

Fig. 17. Same as Fig. 16 but for time average centered at $L_s = 270°$ (northern winter).

at 60°S–90°S from $L_s = 90–120°$ have a larger magnitude than when the VL scheme is used. Consequently, the SOM scheme is able to maintain a latitudinal gradient of Ar mass at 75°S that is nearly double that using the VL scheme. This further demonstrates the ability of the SOM scheme to preserve local tracer gradients without introducing spurious numerical oscillations. Switching the radiative transfer scheme from WBM to KDM significantly increases the strength of tracer fluxes at the southern winter pole, likely because the KDM scheme forces the atmosphere more strongly (consequently increasing the mean overturning circulation and the strength of the southern winter polar vortex). Despite the maximum rate of increase using the KDM scheme being about a factor of two stronger than that using the WBM scheme, the rapid decrease of Ar after $L_s = 120°$ is able to bring the polar Ar back to its homogeneously mixed state by spring equinox. Another notable difference is that the outflow of Ar away from the pole at 75°S from $L_s = 90°$ to $L_s = 120°$ is significantly reduced using the KDM scheme, while at the same time the rate of decrease of Ar in the north polar region is also reduced. This shows that the KDM scheme does not force a stronger pole-to-pole Ar transport, rather it provides an enhanced polar confinement of Ar in the southern winter vortex. Interestingly, the tracer fluxes in the northern polar region are reduced by a factor of two during northern winter using the KDM scheme, suggesting a weaker poleward transport of Ar. A more intuitive comparison between tracer advection schemes and between radiative transfer schemes can be seen in Fig. 15, where the net flux of Ar in a bin from 75°S to 90°S is shown. The flux is strongest for the KDM scheme, followed by the SOM scheme and then the VL scheme, both using the WBM scheme. The polar flux transports, once time integrated, explain the differences in the Ar enhancement factor among these three cases shown in Fig. 11.

To illustrate how mean and eddy transport can affect the polar Ar fluxes, we decompose the total fluxes into mean and eddy parts as described in Eq. (17) and for $L_s = 90°$ and $L_s = 270°$ (Figs. 16 and 17). Both the mean meridional and eddy components of Ar transport exhibit sign differences between the two solstices. The relative importance of the transports determines the amount of Ar being trapped in the polar regions. The mean meridional circulation is responsible for the inflow of Ar into the south pole during southern winter and north pole during northern winter, while eddy transport counteracts it. Referring to the zonal mean meridional circulations (Fig. 8), the cross-equatorial overturning circulations rise in the summer hemisphere and descend in the winter hemisphere. Ar carried by the descending branches of these cells is transported poleward by polar cells. This together with the return flow of the cross-equatorial circulation creates a divergence of Ar fluxes at 60° latitude and near the surface in both winter hemispheres. Eddy transport, on the other hand, is confined to a thin, near-surface layer (several tens of pascals) in the polar regions and actively removes Ar from the poles with relatively weaker strength. The net effect of these two transport processes is to accumulate Ar mass near the surface in polar regions. At the same time, Ar fluxes associated with the ascending branches of the polar cells and the upper part of the poleward cross-equatorial circulations converge between 1 Pa and 10 Pa (along the dotted lines that depict zero fluxes in Fig. 18), which creates a local maximum Ar

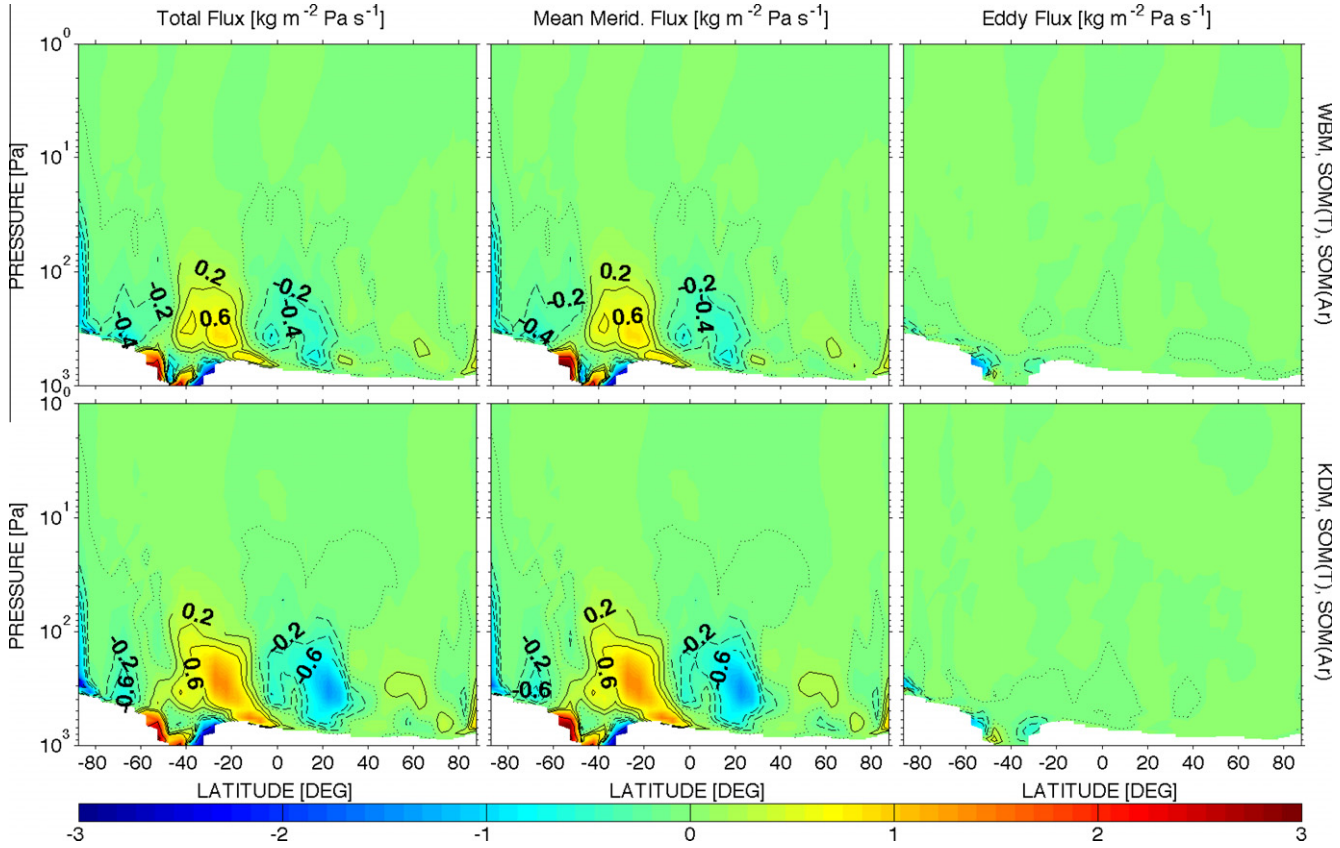

Fig. 18. Same as Fig. 16 but for zonal mean vertical fluxes of Ar. Note the vertical velocity is in unit of Pa s^{-1}. The dashed lines with bluish color are upward fluxes and the solid lines with reddish color are downward fluxes.

mmr that is further enriched when local CO_2 condensation occurs (Fig. 13).

Isolating the zonal mean and eddy fluxes of Ar also helps us to identify the roles of tracer advection schemes and radiative transfer schemes on the tracer distribution. In our studies, we find that the former affects both the mean and eddy transport while the latter appears to have a significant impact only on the mean meridional transport. By taking the difference of each component in Eq. (17) between the SOM and VL tracer advection schemes,

$$\Delta\left([\overline{v}\overline{q}]\frac{\Delta p}{g}\right) = [\overline{v}\overline{q}]\frac{\Delta p}{g}\Big|_{SOM} - [\overline{v}\overline{q}]\frac{\Delta p}{g}\Big|_{VL}$$

we find the SOM scheme moderately increases both the poleward zonal mean fluxes and the equatorward eddy fluxes along the slopes of the topography, which can be seen as more positive and more negative in the south polar region during southern winter (and adversely in north polar region during northern winter) in Fig. 19. Such a difference does not exist at mid-to-low latitudes where $\Delta\left([\overline{v}\overline{q}]\frac{\Delta p}{g}\right)$ is very small. The net effect of these two transport components is to increase the total tracer flux into the south pole during southern winter and north pole during northern winter. The coincidence between the locations where the effect of advection schemes is large and where the eddy activity is strong suggests that the choice of tracer advection schemes may have a greater impact on tracer transport on scales closer to those of the grid spacing than those on a more planetary scale (*i.e.* have greater impact for eddies and where gradients of tracer, heat, and/or wind are sharpest).

Further comparison of tracer transport between the WBM and KDM radiative transfer schemes shows the zonal mean meridional fluxes at mid-to-low latitudes in the KDM simulation to be about a factor of two larger than those in the WBM simulations during both winter seasons. The larger cross-equatorial mean transport of Ar in the KDM simulation is due to the elevated temperatures above 100 Pa (Fig. 6), which force a stronger thermally-direct tropical mean overturning circulation in all seasons. The mean meridional tracer transport near the winter poles behaves quite differently between these two radiative transfer schemes. The poleward Ar fluxes in the KDM simulation are stronger and more confined to the near surface layer (deeper blue[1] color depth 60°S–90°S in Fig. 16) during southern winter, while their counterparts in the northern polar region are significantly weaker during northern winter (Fig. 17). The eddy fluxes at the winter poles, however, exhibit very similar strength in both the WBM and KDM simulations despite different polar dynamics. As a result, the KDM simulation produces more Ar mass at the southern winter pole and less at the northern winter pole (Fig. 14).

Given the suggestion by Nelli et al. (2007) and Colaprete et al. (2008), it is perhaps surprising to see that our model does not produce a local maximum eddy mixing of Ar away from the poles near 50 Pa, where the transient eddy activity is expected to be strong. Banfield et al. (2004) analyzed atmospheric traveling waves in the MGS TES data and found them to show strong seasonal variability. Eddy activities (characterized by temperature perturbations) associated with these waves were seen at high latitudes with a local maximum near 50 Pa, and they were stronger during northern winter than their counterparts during southern winter. We see similar behavior in our model but only for temperature.

[1] For interpretation of color in Figs. 1, 3, 5–7, 9–14, 16–19, and A1, the reader is referred to the web version of this article.

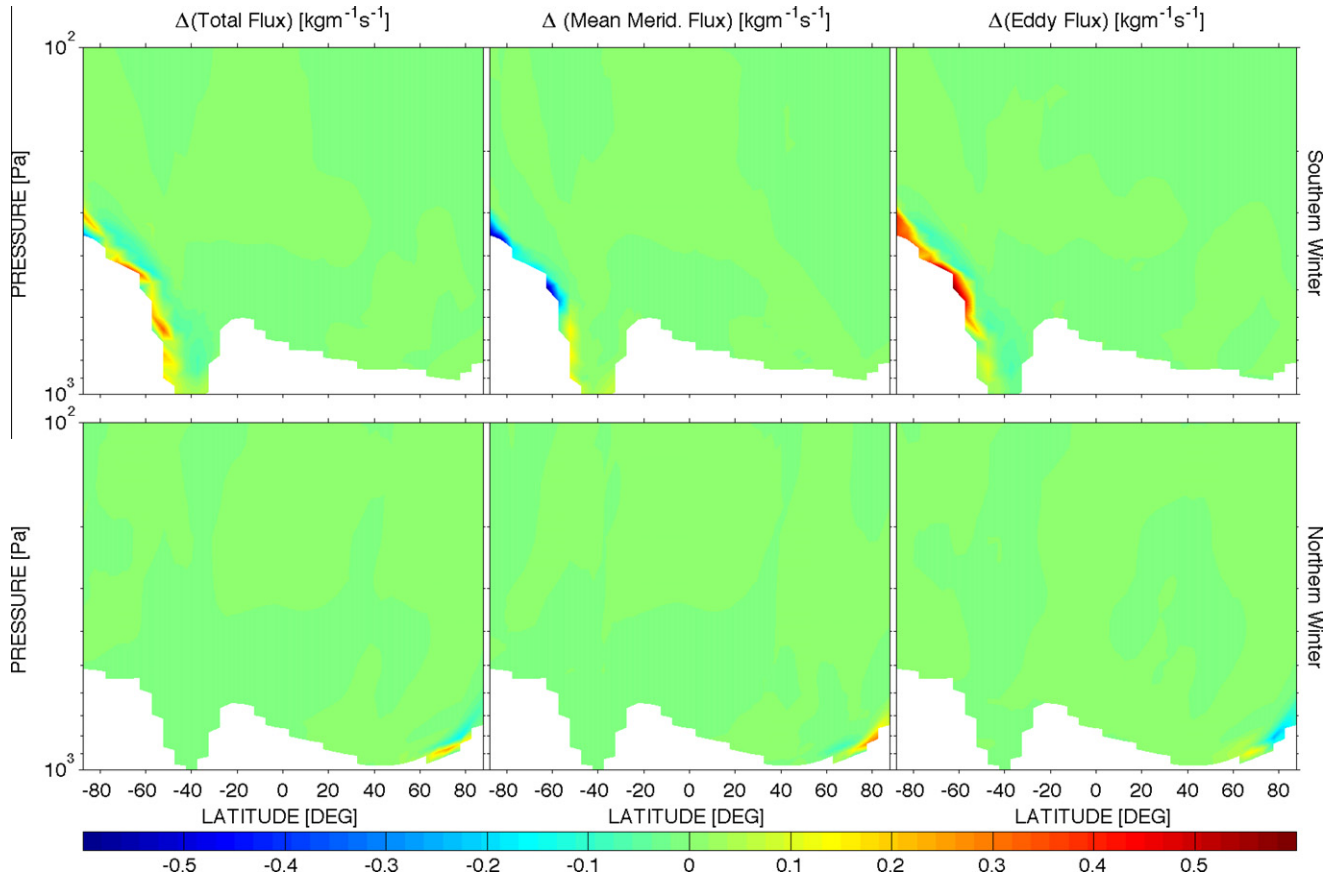

Fig. 19. Differences of the total (left column), advective (center column) and eddy fluxes (right column) of Ar for the WBM simulations with the SOM temperature and VL tracer advection schemes and the WBM with the SOM temperature and SOM tracer advection schemes. The zonal mean fluxes are time averaged over 60° of the solar longitude centered at $L_s = 90°$ (top row) and at $L_s = 270°$ (bottom row).

The separation in altitude between the strongest eddy transport of temperature and Ar in our model is primarily due to the rapid decay of Ar abundance away from the surface. During southern winter (Figs. 12 and 13), Ar is highly concentrated near the surface where a small perturbation in the wind field can cause a large mixing of Ar (Fig. 16). Furthermore, a second local maximum of Ar abundance that appears near several pascals is well beyond the reach of the strong eddy activity. During northern winter, Ar abundance is still highest near the surface but decreases more rapidly with altitude than in the south during southern winter. The majority of the Ar is limited to the region from the surface up to 200 Pa at the northern winter pole (not shown). In both scenarios eddy mixing of Ar is thus relatively weak near 50 Pa. We suspect that the above-described vertical distribution of Ar is an important part of our producing an overall higher enhancement factor at the southern winter pole compared to that in the NASA Ames GCM. Additionally, Nelli et al. (2007) pointed out the polar filter designed to maintain numerical stability (see Section 2.8) could affect polar Ar abundance by up to 30% in the NASA Ames GCM, suggesting a strong diffusive mixing of Ar which is greatly reduced using our cube–sphere grid for which no polar filter is required.

4. Conclusion and discussion

Current Mars GCMs do a very poor job in fitting the magnitude of argon enhancement observed during southern autumn and winter over the winter pole (Sprague et al., 2007). This is likely partially due to errors in physical representation of CO_2 in models and errors in model forcing, but it also seems likely that current Mars GCMs do not represent transport sufficiently well. Indeed, a major argument in the generation of the argon retrievals was to provide the "cleanest" possible data set with which to test dynamical models. In this study, we have implemented a new GCM designed to provide better representation of dynamics, both through an improved numerical treatment of spatial discretization and through the availability of sophisticated in-line tracer transport schemes. We have used the model to study Ar enhancement, examining the sensitivity of the results to the choice of tracer transport scheme and the radiative forcing. We have also assessed model behavior regarding the eddy and mean meridional transport, and the relationship between these transport modes and the location of CO_2 condensation in the atmospheric column.

We have developed a new Mars GCM (the Ashima/MIT Mars GCM) by combining our existing MarsWRF physics packages with the MITgcm to take advantage of the flexibility and conservation properties of the latter's finite-volume dynamical core. Our new GCM produces zonal mean temperature fields that compare well with MGS TES and MRO MCS observations for all seasons. We are also able to reproduce a seasonal CO_2 cycle that closely matches the surface pressure measurements at Viking Lander 1 and 2. Further inter-model comparison shows that the overall performance of our model to be on par with or better than other popular Mars GCMs. More specifically, the Ashima/MIT Mars GCM shows a significant improvement in tracer transport over other Mars GCMs in terms of its ability to reproduce the GRS-derived polar enhancement of non-condensable tracer during southern winter on Mars.

To investigate potential reasons behind the common failure to predict the large Ar EF observed at the southern winter pole, we have performed extensive case sensitivity studies on advection

schemes, which have not received attention to date in Mars GCM development. Our simulation results suggest that the quality of both temperature and tracer advection affects the temporal and spatial tracer distributions, and that the variation of EF among all combinations of schemes can be as high as 35%. For a given temperature advection scheme, we find a clean trend of Ar enhancement among all the tracer advection schemes tested at the southern winter pole, where using the SOM advection scheme produces the highest EF, followed by the OSMP, VL and 3rd UW schemes. For a given tracer advection scheme, varying temperature advection schemes yields non-trivial changes, largely because of the complex response of the atmospheric circulation and the tracer distribution to temperature advection schemes. For instance, the temperature advection schemes can modify the temperature field (hence the dynamics) and the locations of CO_2 condensation, which consequently changes the local tracer abundance as well as the tracer advection. Nonetheless, we are able to identify an optimal combination of advection schemes: the SOM scheme used for both temperature and tracer advection produces the largest Ar EF, reaching a maximum value of $\sim$4 in combination with our initial radiative transfer scheme (the WBM scheme) but still $\sim$35% smaller than the observed.

The use of the more sophisticated KDM radiative transfer scheme with the SOM temperature and tracer advection schemes provides the most satisfactory result for Ar enhancement. This simulation produces a maximum south polar EF of $\sim$4.75 peaking at $L_s = 120^\circ$ during southern winter. The timing and magnitude of this peak value represent the best model match to the GRS observations during MY26 yet published for any GCM. The improved EF is a result of a more strongly forced atmosphere with the KDM scheme (vs. the WBM scheme), which consequently modifies the atmospheric circulation patterns and local CO_2 condensations without degrading the quality of the CO_2 cycle. This is a strong indication that, in order to quantitatively reproduce the observed non-condensable tracer distribution, both the circulation and tracer transport processes must be modeled correctly in GCMs.

We performed a mean and eddy diagnostic analysis of the model simulations in an effort to identify the mechanisms that control the enrichment and dilution of Ar in the polar regions, as well as to isolate the roles of advection schemes and radiative forcing on the tracer distribution. We find that the mean meridional fluxes are responsible for transporting Ar into the pole while eddy fluxes take Ar away from the pole. The net flux transport is stronger towards the southern winter pole and weaker towards the northern winter pole, which explains the dichotomy of Ar enhancement (or Ar mass) between the two winter poles. These principle results are consistent with previous studies (Nelli et al., 2007). Further investigation suggests the advection schemes affect both mean and eddy transport but primarily in the regions where eddy activity is strongest. The ability of a tracer advection scheme to maintain horizontal gradients of the tracer field appears to be a key to producing higher Ar concentration in polar regions. Analysis of the impact of different radiative transfer schemes, on the other hand, indicates a strong influence of radiative forcing on the mean transport, but suggests that the differences in eddy transport are negligible. The KDM scheme produces stronger mean meridional transport at mid-to-low latitudes and at the southern winter pole, while the WBM scheme produces stronger mean transport at the northern winter pole. The resulting EF values due to the differences in mean meridional tracer transport are about 50% larger using the KDM scheme at the southern winter pole and about 20% smaller using the KDM scheme at the northern winter pole.

Seeing that the advection schemes have a significant influence on tracer transport, one may ask if there is a best advection scheme we should always use in the Ashima/MIT Mars GCM and in other GCMs? If not, is it possible to establish criteria to select the most appropriate advection scheme for a particular situation? It appears that the SOM advection scheme performs the best in our model. A recent study of tracer transport in eddying flows using the MITgcm (Hill et al., 2012) shows that the SOM advection scheme is able to suppress spurious diapycnal mixing in the ocean to levels below those of field measurements, while other linear and nonlinear advection schemes produce larger effective diffusivities. This further encourages the use of the SOM advection scheme when eddy activity is strong. However, Hourdin and Armengaud (1999) found that the VL scheme performed similarly to the SOM scheme in their *Radon cycle* experiments with LMD model, where the VL scheme showed its superiority in capturing more grid-scale information than higher-order moment schemes such as the SOM scheme when spatial resolution is rather coarse. Their results conflict with ours, where the VL scheme is even outperformed by a more diffusive 3rd order UW scheme. These results suggest we may be able to find a best advection scheme for any one type of simulation, but it may not be universally applicable when shifting dynamical regimes and/or changing the grid resolution. Clearly more work is needed on studying the impact of tracer transport representation in Mars GCMs.

Despite the peak value of EF resulting from this study being much closer to GRS observations than any previous model, EF values in our model are still generally smaller during most of the winter season. This suggests our model does not capture all of the physics and dynamics related to Ar enhancement. One missing aspect is the molecular mass effect of non-condensable tracers. It is commonly assumed that non-condensable tracers are passive and do not affect the dynamics. This assumption provides a good approximation when the tracer abundance is low. However, during winter in the southern polar atmosphere, non-condensable tracers 'freeze distilled' by the condensation of CO_2 can be greatly enriched; consequently the local CO_2 partial pressure is reduced thus the CO_2 frost temperature is lowered. Forget et al. (2009) further suggests the local depletion of CO_2 can reduce the surface thermal infrared cooling by as much as 5%. Additionally, the enrichment of lighter non-condensable trace gas such as N_2 reduces the mean mass density locally, causing buoyant vertical mixing of tracers. If this vertical mixing were strong, it would effectively transport tracers to higher altitudes where the meridional eddy mixing is weak so an even larger EF may be achieved. However, our tentative experiments with the inclusion of variable mean molecular mass contributions from Ar and N_2 suggest that the lowered local CO_2 partial pressure (equivalently the lowered frost temperature) significantly reduces the amount of CO_2 condensation at winter poles, which in turn reduces the column integrated tracer mmr. At the same time, the buoyant vertical mixing is much weaker comparing to the mean transport of tracer by the polar cells. The net effect of mean molecular mass is thus to reduce the Ar enhancement factor by about 40%.

An alternative convective forcing source is CO_2 moist convection, which is far more rapid than any vertical mixing induced by changes in the mean molecular mass. Colaprete et al. (2008) showed that the polar night CO_2 convection can effectively carry tracers to higher altitudes, well above 50 Pa, where eddy mixing is absent, and provided a possible mechanism to further increase the polar Ar enhancement. Furthermore, our studies suggest the modeled temperature field has a huge impact on the global tracer transport. It thus follows that one would need to improve the physics parameterization of all radiatively active components (such as dust, water and CO_2 condensation, including their associated microphysical interactions) to produce a completely conclusive result.

Clearly we are a long way from properly understanding and modeling the Ar cycle on Mars, and both dynamical and physical model improvements are likely needed. If only the simulation of

Ar were at stake, we could be forgiven for ignoring our inability to capture its seasonal cycle. However, Ar provides (despite the complexities described here) the simplest possible test of the tracer transport processes that are likely crucial to proper understanding of the water cycle and possibly also the dust cycle on Mars. As a result, study and improved representation of the processes at play within the Ar cycle should greatly benefit the accurate modeling of all aspects of the martian climate system.

Acknowledgments

We wish to thank R.M. Haberle and an anonymous reviewer. During the work described in this paper, we benefited greatly from discussions with F. Forget, X. Guo, S. Nelli and A. Sprague. This work was funded by NASA Planetary Atmospheres under grant number NNX10AB42G to Ashima Research. Simulations were conducted on the NASA HEC Pleiades computer.

Appendix A. Proper scaling for comparison of models with each other and with argon observations

There are two separate issues when attempting to gauge how well models can explain observed spacecraft argon observations: the first is to determine what different model results mean relative to each other; the second is to determine how models at this common comparison reference compare with the data. Here we will first consider how to compare the models, then discuss issues relevant to data comparison.

A.1. Intercomparison of models

Including the Ashima/MIT Mars GCM described in this paper, there are four Mars GCMs that we would like to compare. The problem of intercomparison revolves around the definition of the enhancement factor (EF). We described the origin of EF in the paper introduction. Its definition is simply the total column argon mass mixing ratio (mmr) at any given point in the model divided by a reference value. The reference value was defined by Sprague et al. (2007) as the VL2 GCMS Ar measurement from $L_s = 135°$. Thus the EF at any model grid point in any model is:

$$\mathrm{EF}(x,y,t) = \frac{\mathrm{Ar}_{mmr}(x,y,t))}{\mathrm{Ar}_{mmr}(\mathrm{VL2}, L_s = 135°)} \quad \text{(A.1)}$$

where $\mathrm{EF}(x,y,t)$ is the enhancement factor at any model latitude (x), longitude (y), or time (t), $\mathrm{Ar}_{mmr}(x,y,t)$ is the total column argon mmr model prediction at any model point and time, and $\mathrm{Ar}_{mmr}(\mathrm{VL2}, L_s = 135°)$ is the model prediction of the argon mmr at the VL2 location and at $L_s = 135°$. Note that the *actual* measurement of argon by the VL2 measurement is not needed.

Strictly speaking, for model intercomparison any common reference location and time could be used for the denominator (so long as it was the same location and season for all models – for example the initial argon or non-condensable gas mmr before the model is allowed to form any carbon dioxide ice would work). However, the definition in Eq. (A.1) has the advantage of then being compatible with the GRS argon measurements themselves.

Unfortunately, none of the published GCM results use the EF definition in Eq. (A.1). For the NASA Ames MarsGCM (Nelli et al., 2007) and the MarsWRF GCM (Guo, 2009), the initial non-condensable mmr is used as the denominator rather than the predicted VL2, $L_s = 135°$ value. This turns out to only have a modest effect (about 20%). Since all the models simulate the carbon dioxide cycle reasonably well, we can calculate a scaling from the Ames and MarsWRF EF values to Eq. (A.1) very easily. The model results shown in Fig. 1 have this "correction" applied.

The LMD Mars GCM scaling is more complex. The values shown in the supplemental materials of Lefèvre and Forget (2009) have been scaled by an arbitrary amount based on arguments presented in Forget et al. (2009). Based on concerns over the validity of the GRS argon measurements, Lefèvre and Forget (2009) and Forget et al. (2009) focused on the general *shape* of the argon enhancement curve over the southern pole rather than on its absolute value. Forget et al. (2009) point out that the maximum modeled EF when calculated to directly simulate the GRS measurements (presumably with an equation like Eq. (A.1)) is roughly 3–4. This would place the LMD MarsGCM very comfortably "in family" with the other Mars GCMs at all seasons.

One can independently estimate the LMD MarsGCM EF from Fig. 1c of Lefèvre and Forget (2009). Since the modeled methane and Ar mmr respond essentially identically to enrichment and dilution by the CO_2 cycle (entirely as one would expect, and confirmed in the supplemental material to Lefèvre and Forget (2009)), one can calculate the EF from the CH_4 in Lefèvre and Forget (2009, Fig. 1c). The VL2 (48°N) model prediction at $L_s = 135°$ is roughly mid-way between 9 and 10 ppbv (we take 9.5 ppbv as the value). The model value at $L_s = 0°$ from 75°S to 90°S is between 7 and 9, with most of the area between 8 and 9 ppbv. We take this value to be 8.5 ppbv, and hence derive an $L_s = 0°$ EF for the LMD model for 75°S–90°S of about 0.9. This compares with a value of about EF = 1.75 shown in the supplementary material to Lefèvre and Forget (2009) and Fig. 1 of Forget et al. (2009). From this we can estimate that the values of EF shown for argon by Lefèvre and Forget (2009) and Forget et al. (2009) should be scaled down by a factor of about 1.95 to properly compare with the other GCMs using Eq. (A.1) and with the GRS observations (though see the next section of this appendix). We can also estimate the peak EF to check this scaling. The peak occurs at roughly $L_s = 160°$ in the LMD MarsGCM. The peak CH_4 is just above 50 ppbv within roughly 5° latitude of the pole. However, the band between 75°S and 82.5°S that contributes about 75% of the area poleward of 75°S and is between 20 and 40 ppbv, with most area being between 20 and 30 ppbv. If we hence take the 75°S–90°S value during the peak at $L_s = 160°$ to be about 30 ppbv, then we get a peak EF = 3.2. This compares with a direct scaling of the reported peak of EF = 6 using the 1.95 factor we derived of EF = 3.1. As a result, the LMD Mars GCM output shown in Fig. 1 have been "corrected" by this factor of 1.95.

A.2. Comparison with the argon measurements

The GRS Ar measurements are relative and thus Sprague et al. (2007) calibrated the values against the VL2 lander GCMS measurement at $L_s = 135°$. With this calibration factor, the column mmr and (equivalently) the enhancement factors can be calculated. Forget et al. (2009) has argued that the resulting values are potentially questionable based upon two objections. First, the models show a roughly equal peak factor of depletion in southern summer (roughly 3) to the factor of enhancement they show in winter for the southern pole, while it is argued the GRS data show an enhancement of 6 but a barely measurable dilution. Second, the magnitude of EF = 6 for the southern winter pole is argued to be inconsistent with Alpha Proton X-ray Spectrometer (APXS) result from the Mars Exploration Rovers (Economou, 2008; Arvidson et al., 2011).

Taking the first objection, it seems difficult to determine from the data exactly what the southern polar summer argon dilution factor is (*i.e.* what the observed EF in the southern polar region from roughly $L_s = 240$–$360°$ evaluates to). The data are somewhat noisy, with large error bars and it would seem to us that no specific EF within the range EF = 0–1.5 can strongly be argued for or against at this season based on the data. It does not seem conclusive that there is an offset between models and the data in this period

(see Fig. 1). Not withstanding, it is this offset between dilution and enhancement that Forget et al. (2009) point to as the reason for their scaling of their peak EF from their quoted 3–4 to 6. We note that on purely theoretical grounds, the concentration and dilution of argon over the poles does not have to be centred around unity. A bias towards higher values simply indicates greater isolation of the polar atmosphere over the centre of the cap during the condensing phase in winter and spring than during the sublimation phase in spring and early summer.

The second objection revolves around the idea that an EF = 6 requires all the argon transported to the polar region to be trapped there, and hence there to be no mechanism for the change in the argon mmr that is measured by the APXS in southern autumn and winter (Economou, 2008; Arvidson et al., 2011) (see Fig. A1). Further, we also show two sets of results from the Ashima/MIT Mars GCM that differ in the strength of forcing. Fig. A1 shows that despite a factor of roughly 1.5 difference between the peak southern winter polar EF of 3.5 to almost 5 (between the WBM and KDM Ashima/MIT Mars GCM cases – see body of paper for details of the WBM and KDM runs), both model cases produce equivalently valid (though not identical) season cycles of APXS argon. It seems likely that this is because the area of carbon dioxide condensation throughout much of southern winter is much greater than the circle from 75°S to the pole, and that at these more equatorward latitudes the EF is lower. Hence, perfect containment over the whole seasonal cap is not required by the GRS data. It also more likely a result of the fact that during the southern autumn, the APXS data actually record a dilution of argon mmr resulting from the sublimation of the northern seasonal ice cap. Thus the fact that argon mmr changes at the MER landing sites does not refute a very high degree of southern polar vortex isolation during the early phase of southern cap formation, and especially for the very center of the ice cap.

There are potentially other sources of error in the GRS retrieval of EF relating to the field-of-view offset between GRS and the VL2 calibration point and the fact that it is not clear to what degree the argon enrichment is vertically distributed and how this might effect the peak retrieved EF = 6. However, it is also not clear that the data show obvious signs requiring the recalibration of the GRS argon data by the factor of 30–40% suggested by Forget et al. (2009) or (equivalently) the suggested 'scaling up' of GCM EF values to create equivalent GRS observations, as illustrated in the supplementary material to Lefèvre and Forget (2009) and Fig. 1 of Forget et al. (2009).

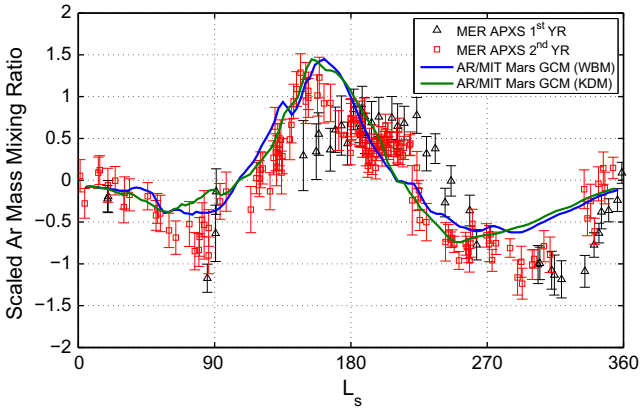

Fig. A1. Opportunity Rover APXS relative argon mmr data and scaled GCM predictions from the Ashima/MIT Mars GCM. Both model cases show a seasonal cycle of argon mmr in reasonable agreement with the APXS data despite the significant difference in the peak southern polar argon enhancement factor (from EF = 3.5 to EF = 4.75). Thus the GCM modeling of APXS does not appear to support the suggestion (Forget et al., 2009) that the existence of seasonal variation in the APXS is inconsistent with the high values of argon EF retrieved from GRS for the southern winter pole.

Appendix B. Tracer enhancement due to local CO_2 condensation

Most Mars GCMs calculate the tracer mixing ratio by assuming all CO_2 condensation events occurring at certain atmospheric levels. This is because they use either η coordinates or σ coordinates in which the layer thicknesses maintain a fixed ratio with respect to the surface pressure, and thus the change of tracer mixing ratio due to local CO_2 condensation cannot be treated automatically by these coordinate systems. Therefore we introduce an algorithm to reconstruct the tracer field according to local CO_2 condensation.

Within one time step, the column mass of non-condensable tracer gases (such as Ar or N_2) does not change before advection takes place. By defining n, $n+\frac{1}{2}$ and $n+1$ as the current time step, an intermediate state and the future time step respectively, we take two steps to reconstruct the tracer field at the future time step as shown in Fig. A2. Note that the intermediate state is not the same as the one used in some time-stepping schemes, rather we use it to describe the state where the tracer mmr changes due to CO_2 condensation (somewhere in the atmosphere) and CO_2 sublimation (in the lowest atmosphere layer). The idea is that first we update the tracer mmr in the layers where CO_2 condensation/sublimation takes place (*i.e*, obtain the tracer distribution in the intermediate pressure grid), then we redistribute the tracer mmr from the intermediate pressure grid to the future pressure grid based on the principle of mass conservation.

It is worth mentioning that the assumed "instant fall" of CO_2 condensates in our model, as opposed to more physical processes such as precipitation and re-evaporation, could introduce uncer-

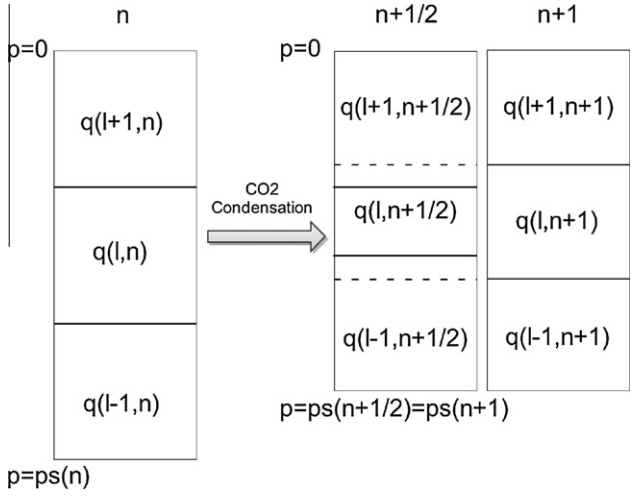

Fig. A2. Demonstration of constructing tracer field after CO_2 condensation in a three-layer atmosphere with equal layer thicknesses. In the diagram, q is the tracer mmr, p is the pressure and p_s is the surface pressure. l is the layer number. n, $n+\frac{1}{2}$ and $n+1$ are the current time step, the intermediate state and the future time step respectively. The dashed lines shown at the intermediate state $n+\frac{1}{2}$ are the actual model grids at the time step $n+1$. Here we consider the case where CO_2 condenses only in the layer l. At the intermediate state, the layer thicknesses (Δp) do not change in the layers $l-1$ and $l+1$ but get thinner in the layer l. Accordingly, the tracer mmrs do not change in the layers $l-1$ and $l+1$ but increase in the layer l. Because we use η coordinates, the atmosphere has equal layer thicknesses at both time steps n and $n+1$. Consequently we need to manually update the tracer mmr (using the mass conservation) to reflect the effect of local CO_2 condensation in the layer l at the future time step $n+1$. In this particular example, the tracer mmrs after CO_2 condensation are: $q_{l+1}^{n+1}=q_{l+1}^{n+\frac{1}{2}}=q_{l+1}^{n}$; $q_{l-1}^{n+1}=q_{l-1}^{n+\frac{1}{2}}=q_{l-1}^{n}$; and $q_{l}^{n+1}=\frac{\Delta p_l^{n+\frac{1}{2}}q_l^{n+\frac{1}{2}}+\left(\Delta p_{l+1}^{n+\frac{1}{2}}-\Delta p_{l+1}^{n+1}\right)q_{l+1}^{n+\frac{1}{2}}+\left(\Delta p_{l-1}^{n+\frac{1}{2}}-\Delta p_{l-1}^{n+1}\right)q_{l-1}^{n+\frac{1}{2}}}{\Delta p_l^{n+1}}$, where $q_l^{n+\frac{1}{2}}=\frac{\Delta p_l^n q_l^n}{\Delta p_l^{n+\frac{1}{2}}}$. The same concept can be used when CO_2 sublimation occurs.

tainties in the following numerical schemes. The effect of the latter on the tracer mmr needs further investigation.

B.1. Pressure and tracer fields at the intermediate state

First, we find the pressure grid in an atmospheric column at the intermediate state and the tracer distribution in this pressure grid right after CO_2 condensation occurs. In our model, CO_2 condensation occurs in the atmosphere whereas CO_2 sublimation only occurs at the surface, as we assume the CO_2 condensates fall instantly to the ground. Conservation of atmospheric mass requires that:

$$\Delta p_1^{n+\frac{1}{2}} = \Delta p_1^n + M^{subl} g - M_1^{cond} g \tag{B.1}$$

$$\Delta p_l^{n+\frac{1}{2}} = \Delta p_l^n - M_l^{cond} g \quad \text{for } l = 2,3,\ldots,N \tag{B.2}$$

where l is the index of layer number from the bottom up, N is the total number of layers in the vertical, Δp_l is the thickness of l_{th} layer, M_l^{cond} (with unit of kg m^{-2}) is the amount of CO_2 condensing out in layer l, M^{sub} (with unit of kgm^{-2}) is the total amount of sublimated ground CO_2 ice, and g is the gravity.

The tracer mmr in each atmospheric layer after CO_2 condensation then becomes

$$q_l^{n+\frac{1}{2}} = q_l^n \frac{\Delta p_l^n}{\Delta p_l^{n+\frac{1}{2}}} \quad \text{for } l = 1,2,\ldots,N \tag{B.3}$$

where q_l is the tracer mmr defined as the ratio between the tracer mass and air mass in layer l.

Once we obtain the layer thicknesses $\Delta p_l^{n+\frac{1}{2}}$ at the intermediate state from Eqs. (B.1) and (B.2), we can build pressure p_e at the edges of the vertical grid as

$$p_{e_1}^{n+\frac{1}{2}} = p_s^{n+\frac{1}{2}} = p_s^n + M^{subl} g - \sum_{l=1}^{N} M_l^{cond} g \tag{B.4}$$

$$p_{e_l}^{n+\frac{1}{2}} = p_{e_{l-1}}^{n+\frac{1}{2}} - \Delta p_{l-1}^{n+\frac{1}{2}} \quad \text{for } l = 2,3,\ldots N+1 \tag{B.5}$$

where p_s^n and $p_s^{n+\frac{1}{2}}$ are the surface pressures at the current time step and the intermediate state respectively.

B.2. Pressure and tracer fields at the future time step

Building the pressure grid at the future time step, *i.e.* the model grid, is very straightforward. Following the definition of η coordinates, the layer thicknesses and the pressure at the edges of the vertical grid at the future time step are

$$\Delta p_L^{n+1} = \Delta p_L^n \frac{p_s^{n+1}}{p_s^n} \quad \text{for } L = 1,2,\ldots,N \tag{B.6}$$

$$p_{e1}^{n+1} = p_s^{n+1} \tag{B.7}$$

$$p_{e_{L+1}}^{n+1} = p_{e_L}^{n+1} - \Delta p_L^{n+1} \quad \text{for } L = 1,2,\ldots,N \tag{B.8}$$

where the surface pressure p_s^{n+1} is the same as $p_s^{n+\frac{1}{2}}$ that is given by Eq. (B.4). Note that we use L as the layer number for the pressure grid p_e^{n+1} to differ from those (l) for the pressure grid $p_e^{n+\frac{1}{2}}$.

The tracer field at the future time step can now be found by fitting the future pressure grid to the intermediate one. We do this from the top down, as the top boundary condition of the model is $p_{eN+1} = 0$. Let us consider a generic case where, for each L, p_{eL}^{n+1} lies between $p_{el(L)}^{n+\frac{1}{2}}$ and $p_{el(L)+1}^{n+\frac{1}{2}}$. Here $l(L)$ is the layer number in the intermediate pressure grid, which satisfies the condition $p_{el(L)}^{n+\frac{1}{2}} \geqslant p_{eL}^{n+1} > p_{el(L)+1}^{n+\frac{1}{2}}$. The tracer field at the future time step can now be constructed as

$$q_N^{n+1} = \frac{\sum_{l=l(N)}^{N} q_l^{n+\frac{1}{2}} \Delta p_l^{n+\frac{1}{2}} - q_{l(N)}^{n+\frac{1}{2}} \left(p_{el(N)}^{n+\frac{1}{2}} - p_{eN}^{n+1} \right)}{\Delta p_N^{n+1}}$$
$$\text{for } p_{el(N)}^{n+\frac{1}{2}} \geqslant p_{eN}^{n+1} > p_{el(N)+1}^{n+\frac{1}{2}} \tag{B.9}$$

$$q_L^{n+1} = \frac{\sum_{l=l(L)}^{N} q_l^{n+\frac{1}{2}} \Delta p_l^{n+\frac{1}{2}} - q_{l(L)}^{n+\frac{1}{2}} \left(p_{el(L)}^{n+\frac{1}{2}} - p_{eL}^{n+1} \right) - \sum_{l=L+1}^{N} q_l^{n+1} \Delta p_l^{n+1}}{\Delta p_L^{n+1}}$$
$$\text{for } p_{el(L)}^{n+\frac{1}{2}} \geqslant p_{eL}^{n+1} > p_{el(L)+1}^{n+\frac{1}{2}}, \text{ and } L = N-1, N-2, \ldots, 2, 1 \tag{B.10}$$

In the numerator of the right-hand side of Eq. (B.10), the first term is the total tracer mass in the layers between $l(L)$ and N at the intermediate state, the second term is the tracer mass in a partial layer between $p_{e_{l(L)}}^{n+\frac{1}{2}}$ and $p_{e_L}^{n+1}$ at the intermediate state, and the third term is the total tracer mass in the layers between $L+1$ and N at the future time step.

Appendix C. Adjustment of physics grid temperatures toward dynamics grid temperatures

The implementation of the physics grid in the η coordinates increases the vertical resolution within the planetary boundary layer (PBL), thus provides better representation of heat exchange between the surface and near-surface atmosphere. However, a caveat is that state variables on the physics grid do not *feel* the dynamics directly, rather they rely on the interpolation/extrapolation from state variables on the coarser dynamics grid. This raises the issue of what is the most accurate and consistent way to interpolate/extrapolate dynamics grid values onto the physics grid. Specifically, how should we adjust the values of temperature across the N physics grid layers that correspond to a single dynamics grid layer?

The method originally adopted in the MITgcm is to adjust the dry static energy, and to do so by shifting all values of dry static energy in the N physics layers by a uniform amount such that their vertically integrated value matches the single value of dry static energy in the corresponding dynamics layer. Although this method is reasonable, it does not consider the distribution of dry static energy on the dynamics grid, thus generally produces large temperature gradients on the physics grid at the edges of the dynamics layers. We therefore introduce a new method to reduce the unphysical thermal structures across the dynamics levels by preserving the vertical temperature gradient between dynamics layers in addition to the total dry static energy.

The conservation of dry static energy in a dynamics layer L with N physics layers in this layer requires an end state

$$\sum_{1}^{N} \left(\theta_f|_{phy}^{l} \Delta p|_{phy}^{l} \right) = \theta|_{dyn}^{L} \Delta p|_{dyn}^{L} \tag{C.1}$$

where

$$\theta_f|_{phy}^{l} = \theta_i|_{phy}^{l} + \delta\theta|_{phy}^{l} \tag{C.2}$$

Here superscript l is the index of physics layer number in a dynamics layer L and subscripts i and f are the initial and final states of potential temperature in physics grid.

It is apparent we need to find the correction term $\delta\theta|_{phy}^{l}$ in Eq. (C.2) under two constraints where dry static energy and temperature gradient are conserved:

$$\sum_{1}^{N} \left(\delta\theta|_{phy}^{l} \Delta p|_{phy}^{l} \right) = \theta|_{dyn}^{L} \Delta p|_{dyn}^{L} - \sum_{1}^{N} \left(\theta_i|_{phy}^{l} \Delta p|_{phy}^{l} \right) \tag{C.3}$$

and for all physics level l in dynamics Level L

$$\left.\frac{\partial T_f}{\partial z}\right|_{phy}^{l} = \left.\frac{\partial T}{\partial z}\right|_{dyn}^{L} \tag{C.4}$$

The MITgm uses potential temperature instead of temperature in η coordinates. Assuming the atmosphere is in hydrostatic equilibrium so that

$$\frac{\partial T}{\partial z} = \frac{g}{c_p} + \frac{g}{R}\frac{\partial ln\theta}{\partial lnp},$$

we can rewrite Eq. (C.4) in terms of potential temperature and pressure as

$$\left.\frac{\partial ln\theta_f}{\partial lnp}\right|_{phy}^{l} = \left.\frac{\partial ln\theta}{\partial lnp}\right|_{dyn}^{L} \tag{C.5}$$

Applying Eqs. (C.2)–(C.5) and assuming we only need a small correction to potential temperature on the physics grid $\left(\delta\theta|_{phy}^{l} \ll \theta|_{phy}^{l}\right)$, we have

$$\left[\frac{1}{\theta_i}\left(1-\frac{\delta\theta}{\theta_i}\right)\frac{\partial\theta_i\left(1+\frac{\delta\theta}{\theta_i}\right)}{\partial lnp}\right]\Bigg|_{phy}^{l} = \left(\frac{\partial ln\theta}{\partial lnp}\right)\Bigg|_{dyn}^{L} \tag{C.6}$$

Ignoring the second order small quantities $O^2\left(\frac{\delta\theta}{\theta_i}\right)$ and after some manipulation we have

$$\left[\frac{\partial\delta\theta}{\partial lnp} - \delta\theta\left(\frac{\partial ln\theta_i}{\partial lnp}\right)\right]\Bigg|_{phy}^{l} = \left(\left.\frac{\partial ln\theta}{\partial lnp}\right|_{dyn}^{L} - \left.\frac{\partial ln\theta_i}{\partial lnp}\right|_{phy}^{l}\right)\theta_i|_{phy}^{l} \tag{C.7}$$

For simplicity, we further take a first order approximation by ignoring the second term on left-hand side of Eq. (C.7)

$$\left(\frac{\partial\delta\theta}{\partial lnp}\right)\Bigg|_{phy}^{l} = \left(\left.\frac{\partial ln\theta}{\partial lnp}\right|_{dyn}^{L} - \left.\frac{\partial ln\theta_i}{\partial lnp}\right|_{phy}^{l}\right)\theta_i|_{phy}^{l} \tag{C.8}$$

Solutions of Eqs. (C.3) and (C.8) give the correction term $\delta\theta|_{phy}^{l}$ we are looking for.

Finally we construct a discretized form of Eqs. (C.3) and (C.8) by taking the center-to-center gradient of potential temperature on both the dynamics and physics grid for all $l = 2, 3, \ldots, N$

$$\begin{aligned}\delta\theta|_{phy}^{l} - \delta\theta|_{phy}^{l-1} &= \left(lnp|_{phy}^{l} - lnp_{phy}^{l-1}\right)\left(\left.\frac{\partial ln\theta}{\partial lnp}\right|_{dyn}^{\pm L} - \frac{ln\theta_i|_{phy}^{l} - ln\theta_i|_{phy}^{l-1}}{lnp|_{phy}^{l} - lnp|_{phy}^{l-1}}\right)\theta_i^e|_{phy}^{l} \\ &= \Delta\theta|_{phy}^{dyn}(l)\end{aligned} \tag{C.9}$$

where $\theta_i^e|_{phy}^{l}$ is mass weighted potential temperature at the interfaces of physics grid, and

$$\left.\frac{\partial ln\theta}{\partial lnp}\right|_{dyn}^{+L} = \frac{ln\theta|_{dyn}^{L+1} - ln\theta|_{dyn}^{L}}{lnp|_{dyn}^{L+1} - lnp|_{dyn}^{L}} \quad \text{when } p|_{phy}^{l} \leqslant p|_{dyn}^{L} \tag{C.10}$$

$$\left.\frac{\partial ln\theta}{\partial lnp}\right|_{dyn}^{-L} = \frac{ln\theta|_{dyn}^{L} - ln\theta|_{dyn}^{L-1}}{lnp|_{dyn}^{L} - lnp|_{dyn}^{L-1}} \quad \text{when } p|_{phy}^{l} > p|_{dyn}^{L} \tag{C.11}$$

Now we have a system of linear equations with respect to $\delta\theta|_{phy}^{l}$ in each dynamics level L

$$\begin{pmatrix} \Delta p|_{phy}^{1} & \Delta p|_{phy}^{2} & \Delta p|_{phy}^{3} & \cdots & \Delta p|_{phy}^{N} \\ -1 & 1 & 0 & \cdots & 0 \\ & & \cdots & & \\ & & \cdots & & \\ 0 & 0 & \cdots & -1 & 1 \end{pmatrix} \begin{pmatrix} \delta\theta|_{phy}^{1} \\ \delta\theta|_{phy}^{2} \\ \cdots \\ \cdots \\ \delta\theta|_{phy}^{N} \end{pmatrix} = \begin{pmatrix} \theta|_{dyn}^{L}\Delta p|_{dyn}^{L} - \sum_{1}^{N}\left(\theta_i|_{phy}^{l}\Delta p|_{phy}^{l}\right) \\ \Delta\theta|_{phy}^{dyn}(2) \\ \cdots \\ \cdots \\ \Delta\theta|_{phy}^{dyn}(N) \end{pmatrix}$$

The method described here performs very well until we reach the top level of the model domain where the pressure is very low (resulting in a poorly scaled matrix) and using the method of conserving dry static energy would produce an artificial cold top if we inserted the extra physics layers to the uppermost dynamics layer (a procedure originally required by the grid construction in the "GridAlt" package of the MITgcm). This is because some of the extra physics layers could locate above the center of the uppermost dynamics layer where the quantities such as temperature are not defined (*i.e.*, temperatures in these extra physics layers might need to be extrapolated. See Molod (2009) for details). To address this issue, we place these extra physics layers to one layer below the uppermost dynamics layer. In this case, the uppermost physics layer and the uppermost dynamics layer will be identical and all quantities on the physics grid can be interpolated (instead of being extrapolated in some physics layers) using those on the dynamics grid.

References

Adcroft, A., Campin, J., 2004. Rescaled height coordinates for accurate representation of free-surface flows in ocean circulation models. Ocean Model. 7, 269–284.

Adcroft, A., Campin, J.-M., Hill, C., Marshall, J., 2004. Implementation of an atmosphere ocean general circulation model on the expanded spherical cube. Mon. Weather Rev. 132, 2845–2863.

Adcroft, A. et al., 2010. MITgcm User Manual.

Arvidson, R.E. et al., 2011. Opportunity Mars Rover mission: Overview and selected results from Purgatory ripple to traverses to Endeavour crater. J. Geophys. Res. (Planets) 116, E00F15.

Banfield, D., Conrath, B.J., Gierasch, P.J., Wilson, R.J., Smith, M.D., 2004. Traveling waves in the martian atmosphere from MGS TES Nadir data. Icarus 170, 365–403.

Basu, S., Richardson, M.I., Wilson, R.J., 2004. Simulation of the martian dust cycle with the GFDL Mars GCM. J. Geophys. Res. (Planets) 109, 11006–11030.

Briegleb, B.P., 1992. Delta-Eddington approximation for solar radiation in the NCAR community climate model. J. Geophys. Res. (Planets) 97, 7603–7612.

Burk, S.D., 1976. Diurnal winds near the martian polar caps. J. Atmos. Sci. 33, 923–939.

Campin, J.-M., Adcroft, A., Hill, C., Marshall, J., 2004. Conservation of properties in a free-surface model. Ocean Model. 6, 221–244.

Christensen, P.R. et al., 2001. Mars Global Surveyor Thermal Emission Spectrometer experiment: Investigation description and surface science results. J. Geophys. Res. 106, 23823–23872.

Colaprete, A., Barnes, J.R., Haberle, R.M., Montmessin, F., 2008. CO_2 clouds, CAPE and convection on Mars: Observations and general circulation modeling. Planet. Space Sci. 56, 150–180.

Collins, M., Lewis, S.R., Read, P.L., Hourdin, F., 1996. Baroclinic wave transitions in the martian atmosphere. Icarus 120, 344–357.

Daru, V., Tenaud, C., 2004. High order one-step monotonicity-preserving schemes for unsteady compressible flow calculations. J. Comput. Phys. 193, 563–594.

Economou, T.E., 2008. Mars atmosphere argon density measurement on MER mission. LPI Contrib. 1447, 9102–9104.

Edwards, J.M., Slingo, A., 1996. Studies with a flexible new radiation code. I: Choosing a configuration for a large-scale model. Q. J. R. Meteorol. Soc. 122, 689–719.

Engquist, B., Sjögreen, B., 1998. The convergence rate of finite difference schemes in the presence of shocks. SIAM J. Numer. Anal. 35, 2464–2485, <http://dl.acm.org/citation.cfm?id=305653.305672>.

Farmer, C.B., Davies, D.W., Laporte, D.D., 1976. Viking: Mars atmospheric water vapor mapping experiment – Preliminary report of results. Science 193, 776–780.

Forget, F. et al., 1999. Improved general circulation models of the martian atmosphere from the surface to above 80 km. J. Geophys. Res. 104, 24155–24176.

Forget, F., Wanherdrick, Y., Lewis, S.R., 2001. Validation of the Mars General Circulation Model and climate database with new spacecraft observations. In Work Package 7, Tech. Note 11369/95/nl/jg. Eur. Space Agency, Paris.

Forget, F., Millour, E., Montabone, L., Lefevre, F., 2009. Noncondensable gas enrichment and depletion in the martian polar regions. In: Third International Workshop on Mars Polar Energy Balance and the CO_2 Cycle. LPI Contributions 1494, pp. 15–16.

Fox-Rabinovitz, M.S., Stenchikov, G.L., Suarez, M.J., Takacs, L.L., 1997. A finite-difference GCM dynamical core with a variable-resolution stretched grid. Mon. Weather Rev. 125, 2943–2968.

Garvin, J.B., Frawley, J.J., Abshire, J.B., 1999. Vertical roughness of Mars from the Mars Orbiter Laser Altimeter. Geophys. Res. Lett. 26, 381–384.

Gregory, A.R., West, V., 2002. The sensitivity of a model's stratospheric tape recorder to the choice of advection scheme. Q. J. R. Meteorol. Soc. 128, 1827–1846.

Guo, X., 2009. Modeling Studies Related to Carbon Dioxide Phase Change on Mars. Dissertation (PhD). California Institute of Technology.

Guo, X., Lawson, W.G., Richardson, M.I., Toigo, A., 2009. Fitting the Viking Lander surface pressure cycle with a Mars General Circulation Model. J. Geophys. Res. (Planets) 114, 7006–7024.

Haberle, R.M., Leovy, C.B., Pollack, J.B., 1982. Some effects of global dust storms on the atmospheric circulation of Mars. Icarus 50, 322–367.

Haberle, R.M. et al., 1993. Mars atmospheric dynamics as simulated by the NASA Ames General Circulation Model. I – The zonal-mean circulation. J. Geophys. Res. 98, 3093–3123.

Haberle, R.M. et al., 2008. The effect of ground ice on the martian seasonal CO_2 cycle. Planet. Space Sci. 56, 251–255.

Heavens, N.G., McCleese, D.J., Richardson, M.I., Kass, D.M., Kleinböhl, A., Schofield, J.T., 2011a. Structure and dynamics of the martian lower and middle atmosphere as observed by the Mars Climate Sounder: 2. Implications of the thermal structure and aerosol distributions for the mean meridional circulation. J. Geophys. Res. (Planets) 116, E01010.

Heavens, N.G. et al., 2011b. The vertical distribution of dust in the martian atmosphere during northern spring and summer: Observations by the Mars Climate Sounder and analysis of zonal average vertical dust profiles. J. Geophys. Res. (Planets) 116, E04003.

Hill, C., Ferreira, D., Campin, J., Marshall, J., Abernathey, R., Barrier, N., 2012. Controlling spurious diapycnal mixing in eddy-resolving height-coordinate ocean models: Insight from virtual deliberate tracer release experiments. Ocean Model 45–46, 14–26.

Hong, S., Pan, H., 1996. Nonlocal boundary layer vertical diffusion in a medium-range forecast model. Mon. Weather Rev. 124, 2322–2339.

Hourdin, F., 1992. A new representation of the absorption by the CO_2 15-microns band for a martian general circulation model. J. Geophys. Res. (Planets) 971, 18319–18335.

Hourdin, F., Armengaud, A., 1999. The use of finite-volume methods for atmospheric advection of trace species – Part I: Test of various formulations in a general circulation model. Mon. Weather Rev. 127, 822–837.

Iselin, J.P., Gutowski, W.J., Prusa, J.M., 2005. Tracer advection using dynamic grid adaptation and MM5. Mon. Weather Rev. 133, 175–187.

Johnson, S.S., Mischna, M.A., Grove, T.L., Zuber, M.T., 2008. Sulfur-induced greenhouse warming on early Mars. J. Geophys. Res. (Planets) 113, E08005.

Kahre, M.A., Haberle, R.M., 2010. Mars CO_2 cycle: Effects of airborne dust and polar cap ice emissivity. Icarus 207, 648–653.

Kelly, N.J. et al., 2006. Seasonal polar carbon dioxide frost on Mars: CO_2 mass and columnar thickness distribution. J. Geophys. Res. (Planets) 111, E03S07.

Lee, C. et al., 2011. Demonstration of ensemble data assimilation for Mars using DART, MarsWRF, and radiance observations from MGS TES. J. Geophys. Res. (Planets) 116, 11011–11027.

Lefèvre, F., Forget, F., 2009. Observed variations of methane on Mars unexplained by known atmospheric chemistry and physics. Nature 460, 720–723.

Leovy, C., 2001. Weather and climate on Mars. Nature 412, 245–249.

Leovy, C., Mintz, Y., 1969. Numerical simulation of the atmospheric circulation and climate of Mars. J. Atmos. Sci. 26, 1167–1190.

Lewis, S.R. et al., 1999. A climate database for Mars. J. Geophys. Res. (Planets) 1042, 24177–24194.

Lian, Y., Showman, A.P., 2010. Generation of equatorial jets by large-scale latent heating on the giant planets. Icarus 207, 373–393.

Lin, S.J., Rood, R.B., 1996. Multidimensional flux-form semi-Lagrangian transport schemes. Mon. Weather Rev. 124, 2046–2070.

Lomax, H., Pulliam, T.H., Zingg, D.W., 2001. Fundamentals of Computational Fluid Dynamics. Springer.

López-Valverde, M.A., Edwards, D.P., López-Puertas, M., Roldán, C., 1998. Non-local thermodynamic equilibrium in general circulation models of the martian atmosphere: 1 – Effects of the local thermodynamic equilibrium approximation on thermal cooling and solar heating. J. Geophys. Res. 1031, 16799–16812.

Marshall, J., Hill, C., Perelman, L., Adcroft, A., 1997. Hydrostatic, quasi-hydrostatic, and nonhydrostatic ocean modeling. J. Geophys. Res. 102, 5733–5752.

Marshall, J., Adcroft, A., Campin, J.-M., Hill, C., White, A., 2004. Atmosphere ocean modeling exploiting fluid isomorphisms. Mon. Weather Rev. 132, 2882–2894.

McCleese, D.J. et al., 2008. Intense polar temperature inversion in the middle atmosphere on Mars. Nat. Geosci. 1, 745–749.

McCleese, D.J. et al., 2010. Structure and dynamics of the martian lower and middle atmosphere as observed by the Mars Climate Sounder: Seasonal variations in zonal mean temperature, dust, and water ice aerosols. J. Geophys. Res. (Planets) 115, E12016.

Mellon, M.T., Jakosky, B.M., Kieffer, H.H., Christensen, P.R., 2000. High-resolution thermal inertia mapping from the Mars Global Surveyor Thermal Emission Spectrometer. Icarus 148, 437–455.

Molod, A., 2009. Running GCM physics and dynamics on different grids: Algorithm and tests. Tellus A 61, 381–393.

Montmessin, F., Forget, F., Rannou, P., Cabane, M., Haberle, R.M., 2004. Origin and role of water ice clouds in the martian water cycle as inferred from a general circulation model. J. Geophys. Res. (Planets) 109, E10004.

Nelli, S.M. et al., 2007. Dissecting the polar dichotomy of the noncondensable gas enhancement on Mars using the NASA Ames Mars General Circulation Model. J. Geophys. Res. (Planets) 112, E08S91.

Newman, C.E., Lee, C., Lian, Y., Richardson, M.I., Toigo, A.D., 2011. Stratospheric superrotation in the TitanWRF model. Icarus 213, 636–654.

Owen, T., Biemann, K., Biller, J.E., Lafleur, A.L., Rushneck, D.R., Howarth, D.W., 1977. The composition of the atmosphere at the surface of Mars. J. Geophys. Res. 82, 4635–4639.

Peixoto, J.P., Oort, A.H., 1992. Physics of Climate. American Institute of Physics (AIP), New York.

Prather, M.J., 1986. Numerical advection by conservation of second-order moments. J. Geophys. Res. 91, 6671–6681.

Prettyman, T.H., Titus, T.N., 2004. Exploring martian polar atmospheric circulation and surface interactions. EOS Trans. 85, 403–404.

Randall, D.A., 2000. General Circulation Model Development: Past, Present, and Future. Academic Press, 807pp..

Read, P.L., Thomas, N.P.J., Risch, S.H., 2000. An Evaluation of Eulerian and semi-Lagrangian advection schemes in simulations of rotating, stratified flows in the laboratory. Part I: Axisymmetric flow. Mon. Weather Rev. 128, 2835–2852.

Richardson, M.I., Wilson, R.J., 2002a. A topographically forced asymmetry in the martian circulation and climate. Nature 416, 298–301.

Richardson, M.I., Wilson, R.J., 2002b. Investigation of the nature and stability of the martian seasonal water cycle with a general circulation model. J. Geophys. Res. (Planets) 107, 5031–5058.

Richardson, M.I., Toigo, A.D., Newman, C.E., 2007. PlanetWRF: A general purpose, local to global numerical model for planetary atmospheric and climate dynamics. J. Geophys. Res. 112, E09001.

Shapiro, R., 1970. Smoothing, filtering, and boundary effects. Rev. Geophys. Space Phys. 8, 359–387.

Showman, A.P. et al., 2009. Atmospheric circulation of hot Jupiters: Coupled radiative-dynamical general circulation model simulations of HD 189733b and HD 209458b. Astrophys. J. 699, 564–584.

Smith, D.E. et al., 2001. Mars Orbiter Laser Altimeter: Experiment summary after the first year of global mapping of Mars. J. Geophys. Res. 106, 23689–23722.

Sprague, A.L. et al., 2004. Mars' south polar Ar enhancement: A tracer for south polar seasonal meridional mixing. Science 306, 1364–1367.

Sprague, A.L. et al., 2007. Mars' atmospheric argon: Tracer for understanding martian atmospheric circulation and dynamics. J. Geophys. Res. (Planets) 112, 3–17.

Sprague, A.L., Hunten, D.M., Hill, R.E., Rizk, B., Wells, W.K., 1996. Martian water vapor, 1988–1995. J. Geophys. Res. 101, 23229–23254.

Titus, T.N., Colaprete, A., 2005. Mars atmospheric surface interactions and the CO_2 cycle. EOS Trans. 86, 462–465.

Van Leer, B., 1979. Towards the ultimate conservative difference scheme: V – A second-order sequel to Godunov's method. J. Comput. Phys. 32, 101–136.

Wilson, R.J., 1997. A general circulation model simulation of the martian polar warming. Geophys. Res. Lett. 24, 123–126.

Wilson, R.J., Hamilton, K., 1996. Comprehensive model simulation of thermal tides in the martian atmosphere. J. Atmos. Sci. 53, 1290–1326.

Wood, S.E., Paige, D.A., 1992. Modeling the martian seasonal CO_2 cycle: I – Fitting the Viking Lander pressure curves. II – Interannual variability. Icarus 99, 1–27.

Zalucha, A.M., Plumb, R.A., Wilson, R.J., 2010. An analysis of the effect of topography on the martian Hadley cells. J. Atmos. Sci. 67, 673–693.